The *C. elegans* plectin homologue VAB-10 acts as a hemidesmosome mechanosensor

Shashi Kumar Suman[1,2], Csaba Daday[3,4], Teresa Ferraro[1], Thanh Vuong-Brender[1,2,#], Saurabh Tak[1,2], Sophie Quintin[2], François Robin[1], Frauke Gräter[3,4], Michel Labouesse[1,2]*

[1] *Sorbonne Université, CNRS, Institut de Biologie Paris Seine, Laboratoire de Biologie du Développement/ UMR7622,7 Quai St-Bernard, 75005 Paris, France*

[2] *Development and Stem Cells Program, IGBMC, CNRS (UMR7104), INSERM (U964), Université de Strasbourg, 1 rue Laurent Fries, BP10142, 67400 Illkirch, France*

[3] *Interdisciplinary Center for Scientific Computing (IWR), Heidelberg University, Mathematikon, INF 205, 69120, Heidelberg, Germany*

[4] *Heidelberg Institute for Theoretical Studies, Schloß-Wolfsbrunnenweg 35, 69118, Heidelberg, Germany*

 # Present Address: Cell Biology Division, MRC-LMC, Cambridge CB2 0QH, UK

** Correspondance to michel.labouesse@upmc.fr*

Abstract

Mechanical forces control many cellular processes by eliciting mechanotransduction upon changes in tension (mechanosensing). Whereas mechanosensors acting at focal adhesion and adherens junction are known, they remain undefined for hemidesmosomes. Here, we focus on the *C. elegans* plectin homolog VAB-10A, the only evolutionary conserved hemidesmosome component. In *C. elegans*, muscles contractions induce a mechanotransduction pathway in the epidermis involving hemidesmosomes. We used CRISPR to precisely remove spectrin repeats (SR) or a partially hidden Src-homology-3 (SH3) domain within the VAB-10 plakin domain. Deleting the SH3 domain in combination with mutations affecting mechanotransduction, or just part of SR5 shielding the SH3 domain induced embryonic elongation arrest because hemidesmosomes collapse. Notably, recruitment of GIT-1, the first mechanotransduction player, requires the SR5 domain and the hemidesmosome transmembrane receptor LET-805. Interestingly, Molecular Dynamics simulations confirmed that forces acting on VAB-10 relieve the inhibition of the central SH3 domain by the adjacent spectrin repeats. Collectively, our data strongly argue that we identified a hemidesmosome mechanosensor and that the SH3 domain, together with its shielding spectrin repeat, play a key role in mechanosensing.

Introduction

Cells are constantly exposed to various mechanical forces, and their ability to respond is critical for tissue homeostasis, particularly in the context of morphogenesis and cancer progression. For instance during tissue and organ formation, epithelial tissues get strongly deformed due to both cell-intrinsic and cell-extrinsic forces (Gilmour et al., 2017). Yet, cells within the epithelium must maintain cell-cell and cell-matrix cohesion. The adaptation process to these forces relies on mechanosensing and the transduction of specific signals from junctions to the cytoskeleton or to the nucleus (Iskratsch et al., 2014; Ladoux et al., 2015).

Focal adhesions and adherens junctions play a central role in relaying mechanical forces. Tension exerted on those junctions result in similar effects, whereby a protein acting as a junction-linked mechanosensor gets unfolded and recruits additional proteins that either strengthen the junction or induce biochemical signalling (Chen et al., 2017; Moore et al., 2010). Typically, tension applied to focal adhesions can unfold talin, which then recruits vinculin (del Rio et al., 2009), or the adaptor p130Cas, which subsequently activates the small GTPase Rap1 (Sawada and Sheetz, 2002; Sawada et al., 2006). Likewise, α-catenin acts as an adherens junction mechanosensor that also recruits vinculin (le Duc et al., 2010; Yao et al., 2014; Yonemura et al., 2010).

Whereas mechanosensing events occurring at focal adhesions and adherens junctions have now been well characterized (Hu et al., 2017), hemidesmosomes represent another mechano-sensitive junction about which much less is known. In vertebrates, there is evidence that plectin, a core component of vertebrate hemidesmosomes, can mediate the mechanical response of lung epithelial cell when combined with dystroglycan, or can regulate nuclear mechanotransduction in keratinocytes (Almeida et al., 2015; Takawira et al., 2011). In *C. elegans*, we previously found that the hemidesmosome-like junction present in epidermal cells transmits mechanical tension exerted by muscles when they contract (Zhang et al., 2011). *C. elegans*

muscles are positioned along the anterior-posterior axis under the dorso-ventral epidermis (see cross-hatched red lines in Fig. 1A-A'). They are tightly connected to the epidermis through a complex structure acting as trans-epithelial tendons, called fibrous organelles, consisting in two hemidesmosome-like junctions (CeHDs) connected by intermediate filaments (Fig. 1B) (Francis and Waterston, 1991; Gieseler et al., 2017; Vuong-Brender et al., 2016). These structures share the plectin homologue VAB-10A and intermediate filaments with the canonical vertebrate hemidesmosomes (Zhang and Labouesse, 2010a). Due to this tight connection, when muscles contract, they submit dorsal and ventral epidermal cells to mechanical tension. In turn, it initiates a mechanotransduction process in the dorsal and ventral epidermal cells requiring functional hemidesmosomes (Fig. 1A-B) (Zhang et al., 2011). We previously found that the first detectable step in this mechanotransduction process corresponds to the recruitment of the adaptor protein GIT-1 to hemidesmosomes (CeHDs) (Fig. 1C) (Zhang et al., 2011). Building on what is known about mechanotransduction at adherens junctions and focal adhesions (see above), we had predicted that a protein linked to hemidesmosomes should act as a mechanosensor to initiate signalling by recruiting GIT-1 (Zhang et al., 2011).

The goal of the present work was to identify the putative hemidesmosome mechanosensor. Because the only hemidesmosomal protein conserved between *C. elegans* and vertebrates is VAB-10A/plectin (Zhang and Labouesse, 2010a), it was a prime candidate to act as a mechanosensor. To test this possibility, we generated several mutations removing specific domains within VAB-10 and tested their effects on the signaling events associated with the mechanotransduction process elicited by muscle contractions. Our data support the notion that VAB-10 is indeed a mechanosensor, and further reveal a key role for an SH3 protein-protein interaction domain and its spectrin repeat shield in mediating mechanotransduction.

Results

Isolation of novel SH3 and spectrin repeat mutations in *vab-10*

Proteins found at *C. elegans* hemidesmosomes are detailed in Fig. 1B. As outlined above, VAB-10A is a strong mechanosensor candidate as it is the only conserved hemidesmosome protein between *C. elegans* and vertebrates (Zhang and Labouesse, 2010a). Additionally, proteins of the plakin and spectraplakin families such as vertebrate desmoplakin, plectin and MACF/ACF7, *Drosophila* Shot and *C. elegans* VAB-10 contain in their plakin domain up to nine spectrin repeats (SR) (Zhang et al., 2017), which are domains known to unfold *in vitro* under mechanical stress (Law et al., 2003; Lenne et al., 2000) (note that *vab-10* produces two major isoforms through alternative splicing, VAB-10A/plectin and VAB-10B/MACF, which have the plakin domain in common, see below) (Bosher et al., 2003). Furthermore, the central SR harbors a predicted SH3 domain, which could potentially mediate protein-protein interactions (Fig. 1D), although it lacks some critical residues compared to canonical SH3 domains questioning its ability to interact with Pro-rich regions (Choi and Weis, 2011; Ortega et al., 2011).. Indeed, the crystal structure of that region from desmoplakin and plectin suggests that the SH3 domain interacts with the upstream spectrin repeat to stabilize the plakin domain, which should make the SH3 binding region partially occluded and prevented from interacting with other proteins (Fig. 1E) (Choi and Weis, 2011; Ortega et al., 2011). However, recent molecular dynamics simulations (MDS) on plectin and desmoplakin suggested that mechanical force should unfold the two neighboring spectrin repeats to unmask the SH3 domain (Daday et al., 2017). These observations made the plakin domain an attractive candidate to mediate mechanosensing, raising the intriguing possibility that tension could allow the SH3 domain to recruit effectors to initiate mechanotransduction.

We first modeled the equivalent region of VAB-10 on top of Plectin, which showed that its SH3 domain should also be partially masked (Fig. 1E). To functionally test the importance of the plakin domain, we engineered several mutations in *vab-10* by CRISPR-mediated recombination (Fig.

2A-B). Specifically, we introduced a deletion of the first two alpha-helices within the SR5 preceding the SH3 domain, named *vab-10(mc64)* or *vab-10(ΔSR5h1-h2)*, a deletion of the entire SH3 domain named *vab-10(mc62)* or *vab-10(ΔSH3)*, deletions removing SR7 or SR8 - named *vab-10(mc97)* and *vab-10(mc98)*, respectively (or Δ*SR7* and Δ*SR8*) - deletion of the SH3 PSVV residues contributing to ligand binding among canonical SH3 domains, named *vab-10(mc56)*, and several point mutations in conserved SH3 residues or in a cysteine of SR4 predicted to interact with SH3 (Fig. 2A-B, Fig. S1). Our attempts to isolate similar deletions of the other SR domains were unfortunately unsuccessful. By comparison with previously known *vab-10* alleles, *vab-10(ΔSR5h1-h2)* behaved like a strong *vab-10* allele, segregating 100% dead embryos that elongated slightly beyond the 2-fold stage (Fig. 2C-D, Table 1). By contrast, over 90% animals homozygous for *vab-10(ΔSH3)*, deletion of the SH3 PSVV residues, *vab-10(ΔSR7)*, *vab-10(ΔSR8)* were normal, with a few late embryo/arrested larvae displaying a very lumpy morphology (Fig. 2E-G). Other point mutations were homozygous viable with no apparent phenotype (Table S1). In the remainder of this study, we will mainly focus on the SH3 deletion and on the two SR5 alpha-helices preceding the SH3 domain, and briefly mention the results obtained with other mutants.

To facilitate the study of VAB-10, we also generated a CRISPR knock-in of the VAB-10A isoform marked by mCherry at its C-terminus as well as a ΔSH3 version of this knock-in; likewise, we generated a CRISPR knock-in of the other major isoform VAB-10B marked by GFP at the C-ter for the wild-type form, and internally before its SR13 for the ΔSH3 form (Fig. 2I). Homozygous VAB-10A::mCherry and VAB-10B::GFP animals were normal, whereas their ΔSH3 derivatives behaved like *vab-10(ΔSH3)* animals, segregating <10% arrested embryos or L1 larvae (Table 1).

The VAB-10A SH3 domain is essential for mechanotransduction

We first tested whether *vab-10(ΔSH3)* affects the *vab-10A* or *vab-10B* isoforms, we performed complementation tests with the embryonic lethal alleles *vab-10A(ju281)* and *vab-10B(mc44)* (see

Fig. 2I for their positions). The prediction if *vab-10(ΔSH3)* disrupts a specific *vab-10* isoform is that the corresponding trans-heterozygous combination should not be viable or should display serious larval defects, whereas the other trans-heterozygous combination should be normal. In contrast to what we had previously observed when testing the complementation between *vab-10A(e698)* and other *vab-10* alleles (Bosher et al., 2003), we could establish trans-heterozygous *vab-10A(ju281)/vab-10ΔSH3)* and *vab-10B(mc44)/vab-10(ΔSH3)* animals that both segregated between 23% and 29% embryonic lethality and up to 7% strong larval body morphology defects (Fig. 2H). Since homozygous *vab-10A(ju281)* or *vab-10B(mc44)* represent 25% of the progeny, and homozygous *vab-10(ΔSH3)* another 25% of the progeny of which less than 10% display strong defects (see Table1, Fig. 2I), we conclude that *vab-10(ΔSH3)* does not severely compromise VAB-10 function. Since the distribution of the different categories was not statistically different in the progeny of *ju281/mc62* versus *mc44/mc62* trans-heterozygotes, this complementation test alone does not reveal whether *vab-10(ΔSH3)* is a *vab-10A* or *vab-10B* allele, or possibly whether both isoforms might fulfill the function provided by the SH3 domain during embryonic elongation.

We next examined whether the SH3 domain is required to mediate the tensional signal emanating from muscle contractions. We had previously found that mutations in *git-1* or *pak-1* induce high levels of embryonic lethality when combined with the weak allele *vab-10A(e698)*, resulting in compromised hemidesmosomes (Zhang et al., 2011), thereby preventing mechanotransduction to happen.

We tested whether double mutants between *vab-10(ΔSH3)* and *git-1(tm1962)* or *pak-1(ok448)* would induce a similar phenotype. Time-lapse DIC microscopy of *vab-10(ΔSH3)*; *pak-1(RNAi)* or *vab-10(ΔSH3); git-1(tm1962)* embryos showed that they did not progress beyond the 2.5-fold stage (Fig. 3A-B; Movies S1-S3). Specifically, 98% *vab-10(ΔSH3); git-1(tm1962)*, and 100% *vab-10(ΔSH3)*; *pak-1(ok448)* embryos failed to hatch (Fig. 3C; *ok448* removes the kinase domain of PAK-1). These double mutants elongated at a wild-type rate until the 2.2-fold stage, then arrested (Fig. 3A-C). A double mutant combining *vab-10(ΔSH3)* with a mutant removing the

GTPase-binding domain of PAK-1, *pak-1(tm403)*, was not as severely affected (Table 1). We also observed approximately 50% lethality after RNAi against *mec-8* or *crt-1*, two strong enhancers of *vab-10A(e698)* without an embryonic phenotype of their own (Zahreddine et al., 2010) (Table 1). These genetic interactions, together with the type of embryonic arrest, strongly support the notion that *vab-10(ΔSH3)* behaves like a *vab-10A* allele. Finally, we found that *vab-10(ΔSR8)* also induced about 50% embryonic and 40% larval lethality when combined with PAK-1 knockdown and prevented elongation beyond the 2.5-fold (Fig 3A, 3C). By contrast, *vab-10(ΔSR7)* induced less significant lethality when combined with *pak-1(ok448)* (Fig. S1; Table 1). Hence, based on genetic interactions with genes known to mediate mechanotransduction, the SH3 and SR8 domains are important for mechanotransduction. In addition the first part of the SR5 domain is essential for VAB-10 function.

The VAB-10A SH3 domain contributes to maintain hemidesmosome integrity

We had previously found that hemidesmosomes fall apart in most *vab-10A(e698); pak-1(ok448)* double-mutants (Zhang et al., 2011). To define whether *vab-10A(ΔSH3); pak-1(ok448)* embryos arrested elongation for similar reasons, we examined the distribution of LET-805::GFP and MUP-4::GFP, the basal and apical hemidesmosome receptors, respectively. For this, we generated knock-in versions of MUP-4::GFP and LET-805::GFP. After PAK-1 knockdown in the mCherry-tagged *vab-10A(mc62)::mCherry* version (Fig. 2I), hemidesmosomes were normal until the 2-fold stage, and then displayed integrity defects mainly in the region where embryo curvature is the highest (Fig. 4A and Movies S4-S5; see arrows and dotted line in Fig. 4A). Specifically, the LET-805::GFP signal appeared to detach from the outer body wall and to collapse internally as if not held anymore, consistent with the observation that muscles also detached from the body wall (Fig. S2). The basal VAB-10A(mc62)::mCherry signal remained associated with it, but was much dimmer, suggesting that detachment occurred within the epidermis layer (Fig. 4B, bottom three rows and

Movie S6). By contrast, at the apical side, the signal appeared intense although often less compact. These defects, which were not observed in VAB-10(+)::mCherry control embryos after PAK-1 knockdown (Fig. 4B upper row), are strongly reminiscent of those previously observed in *vab-10A(e698); pak-1(ok448)* double mutants (Zhang et al., 2011). These results and the aforementioned genetic interactions raise the hypothesis that the SH3 domain within the VAB-10A/plectin isoform together with PAK-1 are acting in the mechanotransduction process to allow hemidesmosomes to sustain tension beyond the 2-fold stage. This does not preclude an additional role of the SH3 domain within the VAB-10B/MACF isoform. We suggest that hemidesmosomes preferentially rupture in the most convex part of the embryo because tension is higher where the curvature is higher.

VAB-10 and GIT-1 are in close proximity within hemidesmosomes

As mentionned above, we previously established that GIT-1 recruitment to hemidesmosomes is the first detectable step in the mechanotransduction pathway (Fig. 1C). The simplest prediction, whichever protein acts as a mechanosensor upstream of GIT-1 recruitment, is that GIT-1 is in close contact to or physically interacts with this mechanosensor.

To explore this possibility, we used a bi-molecular fluorescence complementation (BiFC) strategy to test if GIT-1 would be located in close proximity to VAB-10A (Hu et al., 2002) (Fig. 5A). We generated CRISPR knock-in strains expressing GIT-1 linked at the C-terminus to the 173 first residues of Venus, and VAB-10A linked at the C-terminus to the last 83 residues of Venus. As a positive control, we co-expressed the same GIT-1::Venus(1-173) and a CRISPR-generated PIX-1::Venus(155-238), since vertebrate Git1 and ß-PIX form a complex (Frank and Hansen, 2008). As shown in Fig. 5B, we found that co-expressing GIT-1::Venus(1-173) with PIX-1::Venus(155-238) or VAB-10A::Venus(155-238) gave a clear hemidesmosomal signal, which was similar to that of endogenous VAB-10A and VAB-10B, and of a novel CRISPR knock-in of GIT-1::GFP (Fig. 5C-D). By

contrast, embryos expressing only one Venus moiety failed to give a signal (Fig. 5B). We conclude that VAB-10A and GIT-1 are located within less than 5-10 nm, the maximum distance beyond which a BiFC signal cannot be detected (Ciruela et al., 2010; Hu et al., 2002). Since the fluorophore moieties were at the C-terminus of each protein, and since VAB-10A is a large protein of 3400 residues, additional methods will be required to define if GIT-1 directly interacts with VAB-10, and with which domain it might do so.

GIT-1 recruitment to hemidesmosomes depends on VAB-10 and LET-805

To further explore the relationship between GIT-1 and hemidesmosomes, we next examined which hemidesmosome component would be required to attract GIT-1. First, we tested whether GIT-1 is still present at hemidesmosomes in the absence of the SH3 domain of VAB-10A. In contrast to the severe reduction of GIT-1::GFP signal observed in embryos defective for the essential muscle protein UNC-112 (Zhang et al., 2011), we found that the GIT-1::GFP signal was unaffected by the absence of the SH3 domain (Fig. 6A). By contrast, absence of the first two helices of the SR5 domain partially reduced GIT-1 recruitment and strongly compromised hemidesmosome integrity where embryo curvature is the highest (line *vab-10(ΔSR5h1-h2)*, Fig. 6A), as previously observed in *vab-10(ΔSH3); pak-1(RNAi)* (see Fig. 4). Since some GIT-1 remained at hemidesmosomes in *vab-10(ΔSR5h1-h2)* mutants, we tested if other hemidesmosome proteins help recruit GIT-1 to hemidesmosomes. To do so, we examined the dynamics of GIT-1::GFP at hemidesmosomes in the absence of LET-805, VAB-10 or PAT-12, three essential hemidesmosomal components (Zhang and Labouesse, 2010a) (Fig. 6A, Movie S7), measuring both the level of GIT-1 and its continuity along the anterior-posterior axis (Fig 6B-B'). We found that GIT-1 levels were reduced and less continuous in all backgrounds, with the following grading in severity: *unc-112(RNAi)* > *let-805(RNAi)* ≥ *vab-10(RNAi)* ≈ *vab-10(ΔSR5h1-h2)* ≥ *pat-12(RNAi)* (Fig. 6C-D). In particular, a strong VAB-10 RNAi knockdown and the deletion of the first two helices of the SR5

domain resulted in very similar phenotypes, whereas *pat-12(RNAi)* moderately affected GIT-1::GFP levels and continuity, while still inducing a strong hemidesmosomal detachment defect (Fig 6, see time +60 min). Importantly, loss of LET-805 does not significantly reduce VAB-10A levels (Hresko et al., 1999), suggesting that LET-805 might be directly involved in recruiting GIT-1. Likewise, we found that *vab-10(ΔSR5h1-h2)* had as strong LET-805::GFP signal, even though it collapsed at the turn (Fig. S3). We conclude that GIT-1 recruitment is likely to involve LET-805 and potentially the VAB-10 SR5 domain.

Biophysical evidence that the SH3 domain can be mechano-sensitive

The previous sections establish that the region shielding the SH3 domain of VAB-10 is essential for mechanotransduction, but that the SH3 domain is unlikely to directly interact with GIT-1. To test by other methods whether this domain can act as a mechanosensitive switch, we used Molecular Dynamics (MD) simulations. Our previous MD simulations of the homologous plakin domains of desmoplakin and plectin under a stretching force have shown that the SH3 domain mechanically stabilizes the spectrin repeats (Daday et al., 2017). Moreover, force relieves the auto-inhibition of the SH3 domain by the preceding SR4 domain, suggesting a mechano-sensing role of the SH3 domain in plakin domains.

We performed the same simulations for a homology model of VAB-10 as shown in Fig. 1E (see Methods). Throughout our equilibrium MD simulation, the contact area between the SH3 domain and the rest of the protein was stable, with quartiles 10.3-11.5 nm^2. This indicates that the VAB-10 SH3 domain interacts with the spectrin repeats in a very similar manner as the previously studied homologue (Daday et al., 2017), and likely has a similar mechano-sensing role as well.

To test this hypothesis, we subjected 10 snapshots from our equilibrium simulations to stretching forces acting on the termini in subsequent force-probe MD simulations. Similar to the tendencies

observed for plectin, we find that the VAB-10 spectrin repeats always unfolded before the SH3 domain, i.e. the SH3 domain was invariably exposed and activated before its unfolding (Fig. S4A-B). This activation could happen at the very first stage of the unfolding of the spectrin region, or in the second stage; hence VAB-10 behaves like plectin and desmoplakin, which we examined in previous simulations (Fig. S4C). In the case of plectin, early activation, that is, after partial unfolding of at most one spectrin repeat, happened in about ⅕ of the simulations, while in the case of VAB-10, this happened even more frequently in ⅓ cases (Fig. 7A). The very similar behavior of the two protein leads us to propose that the SH3 domain found in VAB-10 fulfills, similarly to plectin, a potential dual role: force sensing on the one hand and stabilizing on the other. In agreement, both of these effects can explain the *vab-10A(ΔSH3)* phenotype. We also computationally analyzed the plakin domain of VAB-10 carrying the *ΔSR5h1-h2* deletion (*mc64*), which removes the first two helices of the SR5 spectrin repeat shielding the SH3 domain. Our model predicts the SH3 domain to still bind to the upstream SR4 (Fig. S4D), suggesting that the phenotype induced by the *mc64* deletion is unlikely to result from the permanent availability of the SH3 domain to bind other proteins, and thereby act as a constitutively active protein.

Discussion

This study combines molecular genetic analysis of the *C. elegans* spectraplakin VAB-10/plectin with Molecular Dynamics simulation to functionally test if VAB-10/plectin is a mechanosensor for hemidesmosomes. Our data establish that the plakin domain of VAB-10 is essential to enable mechanotransduction, and that the SH3 domain plays a central role in mechanosensing together with its shielding SR5 spectrin repeat.

The recent crystal structure of the plakin domain of plectin revealed that this domain composed of nine spectrin repeats should adopt an extended rod-like shape (Ortega et al., 2011; Ortega et al., 2016). Intriguingly, it also revealed the presence of an SH3 domain embedded within the central VAB-10 spectrin repeat (SR5). This SH3 is atypical inasmuch it is missing several residues that normally ensure the interaction with Pro-rich target sequences within prototypical SH3 domains. Instead, it exhibits multiple interactions with the previous spectrin repeat SR4, questioning the notion it could act as a *bona fide* SH3 domain (Ortega et al., 2011). By using the power of *C. elegans* molecular genetic tools and CRISPR-mediated recombination approaches, we introduced several point mutations and deletions in the plakin domain of the *C. elegans* spectraplakin VAB-10. Our key findings are that removal of the first two helices of the SR5 domain upstream of the SH3 domain induced severe embryonic elongation defects, but that removal or point mutations within the SH3 domain barely affected VAB-10 function on its own. It is important to stress that the phenotypic differences between the *vab-10(ΔSR5h1-h2)* and alleles affecting the SH3 domain imply that they induce specific effects, and in particular that removal of the SH3 domain does not impair SR5 function. Moreover, the penetrant embryonic lethality induced by *vab-10(ΔSR5h1-h2)* should not solely result from the partial reduction of GIT-1 recruitment, since loss of GIT-1 does not strongly compromise elongation and embryonic viability (Zhang et al., 2011). Strikingly, however, SH3 mutations induced highly penetrant embryonic elongation defects due to the loss of hemidesmosomes in the convex part of the embryo when combined with loss

of the signaling proteins GIT-1 or PAK-1, which form the core of a mechanotransduction process induced by muscles. Importantly, this phenotype is highly reminiscent of the one observed when the weak *vab-10A(e698)* mutation is combined with *pak-1* mutations (Zhang et al., 2011). These genetic results imply that the SH3 domain is important mainly in the VAB-10A isoform to maintain hemidesmosomes.

Genetically speaking, the synergistic effects between VAB-10 SH3 domain (or of SR8 domain) deletion and the knockdown of proteins mediating mechanotransduction (GIT-1, PIX-1 or PAK-1) imply that the SH3 domain is acting in a parallel rather than in a linear pathway with these proteins. Consistent with this conclusion, our fluorescence microscopy analyses showed that GIT-1 was still recruited to hemidesmosomes in the absence of the SH3 domain. Thus, it suggests that a domain distinct from the VAB-10 SH3 domain recruits GIT-1 downstream of the mechanical input provided by muscles, which we demonstrated to be located in close vicinity. Other proteins that could recruit GIT-1 include a VAB-10 domain other than the SH3 (and by the same token other than the SR8), the cytoplasmic domain of the transmembrane receptor LET-805, since GIT-1 level was sharply reduced in its absence (although not as strongly as in the absence of muscle input), or the interface between them. Indeed, we observed that deletion of the first two SR5 alpha-helices – mutation *vab-10(ΔSR5h1-h2)* – reduced the level of GIT-1 at hemidesmosomes, suggesting that it contributes to its recruitment with LET-805. Of note, although *vab-10(ΔSR5h1-h2)* and the presumptive null allele *vab-10(h1356)* reduced GIT-1 recruitment to a comparable level, the former did not affect elongation as strongly as the latter (see Fig. 3C), arguing that *vab-10(ΔSR5h1-h2)* did not completely destabilize VAB-10.

Our Molecular Dynamics simulations predicted that tension should expose the SH3 domain due to the unfolding of the SR4 and/or SR5 domains, and thereby could play a mechanosensing role. Taken together with the results on GIT-1 recruitment, since tension from muscles is not permanent but cyclic (Zhang et al., 2011), one possibility could be that tension promotes the transient GIT-1 recruitment to the unfolded SR4 or SR5 domains, or conversely its unbinding from the folded SR4

or SR5 domains potentially at the interface between VAB-10 and LET-805. Our genetic data further suggest that downstream of the mechanical input provided by muscles, SH3 exposure by mechanical force leads to the activation of signaling proteins distinct from GIT-1/PIX-1/PAK-1, and that it is the combination of both branches that is required to promote embryonic elongation (Fig. 7B).

The paradigm for mechanosensing is largely based on talin and α-catenin, the two best-characterized mechanosensors. In both cases, it occurs when talin and α-catenin interact with a junction receptor (integrin or ß-catenin bound to E-cadherin, respectively) and with actin through specific domains (del Rio et al., 2009; le Duc et al., 2010; Yao et al., 2016; Yao et al., 2014; Yonemura et al., 2010). Receptor activation combined with increased intracellular tension stretches talin or α-catenin to reveal vinculin-binding regions (Hu et al., 2017). How would the VAB-10 based mechanosensing process operate in comparison to talin and α-catenin? Our Molecular Dynamics simulations suggest that stretching the VAB-10 plakin domain can unfold SR4, or less frequently SR5, to make the SH3 domain available for other interactions, as previously observed for plectin and desmoplakin (Daday et al., 2017). Consequently, one could imagine that upon stretching the plakin domain, SR4 or SR5 unfolds, making the SH3 domain available for interaction with signaling factors. We cannot exclude a more complex scenario, whereby the SH3 domain bound to SR4 provides a platform for assembling a signaling complex, and that stretching the plakin domain would a contrario terminate this signaling to possibly initiate another process. In support for the first hypothesis, it has recently been found that the SH3 domain of plectin can bind to microtubule-associated proteins to destabilize their interaction with microtubules (Valencia et al., 2013). In addition, because the muscle-induced mechanical input is intrinsically oscillating, inducing short epidermal areas to be sequentially stretched or compressed several times per minute along the anterior-posterior axis (Zhang et al., 2011), we can imagine that different signaling complexes alternatively bind and unbind to the SR4-bound SH3 and to the free SH3 to facilitate hemidesmosome remodeling.

As recalled above, mechanosensing through talin and α-catenin requires them to bind to a transmembrane receptor and to actin. In the case of VAB-10A, the situation would be conceptually similar although cellularly different. As illustrated in Fig. 1B, there are two hemidesmosome-like structures in the epidermis, one basally and one apically, each associated with a different ECM. Both hemidesmosomes are bridged by intermediate filaments, which together act as tendons linking muscles to the apical ECM. In the 3D space of embryos, when muscles contract in the anterior-posterior direction, this tendon-like structure oriented radially will come under high tension. Although not yet biochemically confirmed, genetic experiments suggest that VAB-10A should bind to the basal transmembrane receptor LET-805 (Bosher et al., 2003; Hresko et al., 1999; Zhang and Labouesse, 2010a), much like plectin binds to ß4-integrin through its two calponin-homology domains and probably the SR4-SR5-SH3 region (Frijns et al., 2012; Koster et al., 2004). It is likewise likely that VAB-10A can bind to MUP-4 on the apical side. While LET-805 basally and MUP-4 apically bear no homology to ß4-integrin, their cytoplasmic tail are long enough to create multiple binding surfaces with VAB-10. Hence, when muscles exert tension on hemidesmosomes, the spectrin repeats of the VAB-10 plakin domain could become unfolded to expose its SH3 domain. There is an intriguing similarity between talin and plakins in that among the 13 alpha helix bundles composing the talin central region, the central one (R8) loops out of the preceding R7 and unfolds with it (Yao et al., 2016), which is partially reminiscent of the SH3 domain being inserted within the central SR5 domain of the plakin domain. Moreover, the Rho GTPase Activating Protein DLC1 (Deleted in Colorectal Cancer1) is active when bound to the folded R8 but becomes inactive and unbound when R8 is unfolded (Haining et al., 2018). Hence, the paradigm emerging from these two junctions is that the cassette mediating mechanosensing appears to involve a domain partially buried within the structure that becomes exposed under mechanical tension.

In conclusion, our work reveals that the architecture of the mechanosensor for hemidesmosomes revealing the key role of plakin domain and its role in mediating the mechanotransduction in

vivo. Molecular Dynamics simulations suggest that the SH3 domain can alternate between an SR4-interacting state and a free state, with the latter being induced by force. Analysis of *C. elegans* embryos suggests that the situation in vivo is complex and could involve multiple protein complexes acting in parallel. By extension, our data suggest that for other spectraplakins too, the SH3 domain and its shielding region are likely to play a critical signaling role in vivo.

Materials and Methods

Strains and culture:

Caenorhabditis elegans wild-type strain and transgenic animals derived from the *N2* strain. They were used for all experiments and maintained as described in (Brenner, 1974). A complete list of strains and associated genotypes used in this study are included in supplementary Table 1.

Molecular Biology:

Plasmid constructions were performed using Standard PCR method (Barstead et al. 1991) and general molecular biological techniques used as described in Sambrook et al. (1989). To construct knock-in DNA plasmid-based repair templates used for CRISPR/Cas9-mediated genome editing, we amplified the >1.5Kb upstream and >500bp downstream sequences from the *N2* genomic DNA, and the fluorophore-encoding fragment from pre-existing vectors by using Phusion DNA polymerase. PCR fragments were analyzed on agarose gel and concentrated by either PCR clean-up or gel purification kit (QIAGEN) and their concentrations measured using a Nanodrop (Eppendorf) before final assembly with pJET1.2 vector using NEBuilder HiFi DNA Assembly Cloning Kit (New England Biolabs). Small Guide encoding plasmids for CRISPR were generated by an overlap extension PCR method performed on template pML2840.

To avoid Cas-9 cleavage of the homologous repair template, the Cas9 site of the repair template was modified by introducing synonymous mutations either directly into the primers used for fragment amplification or separately by Q5 site directed mutagenesis kit (New England Biolabs). All DNA plasmids used for genome editing were transformed into DH5α competent cells and subsequently purified by miniprep (PureLink Quick Plasmid Miniprep Kit (Thermo Fisher Scientific) or Plasmid Midi Kit (QIAGEN). All final DNA constructs were sequence verified before use. The sequences of sg-primers (SIGMA) used in this study are included in Supplementary Table 2.

CRISPR/Cas9-mediated genome editing

Wild type *N2 C. elegans* genetic background was used to generate *vab-10* CRISPR/Cas9 alleles; *let-805* and *mup-4* GFP knock-in strains were generated after injection in an *unc-119(ed3)* background (Dickinson et al., 2013). The sgRNA plasmid, knock-in repair template plasmid, Cas9 encoding plasmid and the appropriate co-injection marker (PRF4/ myo-2::mCherry/ myo-2::GFP) were co-injected into *N2* animals. Typically, injection mixes were prepared in DNase and RNase free MilliQ water and contained a combination of 50-100 ng/μl sgRNA plasmid (targeting specific gene), either 50 ng/μl repair template plasmid or 20-50 ng/μl ssODNA (PAGE-purified oligonucleotide) repair template, and co-injection markers pRF4 [rol-6 (su1006)]100 ng/μl, 2.5 ng/μl myo-2p::mCherry/ myo-2p::GFP. Injection mixes were spun down in a microcentrifuge (Eppendorf) for at least 10-30 minutes at 14,000 RPM prior to use. 30-40 young adult hermaphrodites were injected in the germline using an inverted micro-injection set up (Eppendorf). After injection, one animal per NGM food plate was dispatched and grown at 20 ˚C for 2-3 days. F1 animals carrying co-injection markers were picked and singled out on separate NGM OP50 plate, and grown at 20 ˚C until eggs or larvae were spotted. Each F1 mother was lysed in separate PCR-tube and standard worm PCR protocol was followed using appropriate pairs of primers (annealing in the inserted sequence and a genomic region not included in the repair template). For the construction of some transgenic strains, we also used

Co-CRISPR the *dpy-10* phenotype (Paix et al.,2015) or integration of a self-excisable cassette carrying a visible marker (Dickinson et al., 2015) method. All genotyping experiments were carried out using standard worm PCR method. Confirmed alleles were sequenced and verified (Eurofins).

RNA-mediated interference (RNAi):

RNAi experiments were performed either by feeding on *HT115 Escherichia coli* bacteria strains generating double-stranded RNA (dsRNA) targeting genes of interest or by injection of in-vitro synthesized double-stranded RNA on young L4 stage of the animals. Feeding RNAi clones for *crt-1* and *mec-8* were used from the Ahringer-MRC feeding RNA interference (RNAi) library (Kamath et al., 2003). RNAi feeding was performed using standard procedures, with 100 μg ml^{-1} ampicillin/1 mM IPTG (Sigma). Empty L4440 RNAi vector served as a control. Other experiments involving RNAi were done by injection of dsRNA.

To generate dsRNA for the injection, genomic fragments were PCR amplified using Phusion DNA polymerase (ThermoFisher) and these fragments were further served as templates for in-vitro dsRNA synthesis using T3 or T7 mMESSAGE mMACHINE Kit (Ambion, USA). For gene knockdown experiments by feeding, L4/L1 hermaphrodites were grown on RNAi plates for 24-36 hrs; for dsRNA injection, 20-30 young L4 hermaphrodites were injected with dsRNA targeting gene of interests and grown for 14-20 hrs prior to experiments.

Spinning disk and Nomarski microscopy

For live imaging, embryos were picked from NGM plate by mouth pipette, washed thoroughly in M9 medium and mounted on 2-5% agarose pads after sealing the slides with paraffin oil. Spinning disk imaging of embryos was performed using a Roper Scientific spinning disk system (Zeiss Axio Observer Z1 microscope, Yokogawa CSUX1-A1 spinning disk confocal head,

Photometrics Evolve 512 EMCCD camera, Metamorph software) equipped with a 63X, and 100X oil-immersion objective, NA=1.4. The temperature of the microscopy room was maintained at 20 ˚C. Images of embryos were acquired in either streaming mode with 100 ms exposure, or time-lapse mode with 100 ms exposure and 5 minutes intervals. Laser power and exposure times were kept constant throughout the experiments for specific strains and their control genotypes. For the quantification of hemidesmosomes, images were acquired with 100 ms exposure time in stream mode with 0.3 µm step size. Images were processed and quantified using FIJI. Fluorophores used in this study include eGFP, GFP (65C), mCherry, split VENUS and BFP.

Time-lapse DIC movies were acquired using a Leica DMI6000 upright microscope, a 40X or 63x oil-immersion objective NA=1.25 and a Photometrics Coolsnap HQ2 camera (Photometrics, AZ, US) placed in the temperature-controlled room at 20˚C. For *C. elegans* larvae image acquisition, animals were anesthetized using 0.1 mmol/L levamisole in M9 buffer and mounted on 2% agarose pad.

Homology modelling

We used MODELLER (Sali and Blundell, 1993), version 9.14, through the interface in UCSF Chimera version 1.12 (Pettersen et al., 2004), for homology modelling. Currently, two crystal structures of proteins with SH3 insertions are available: 3PE0 (plectin) and 3R6N (desmoplakin). The main difference between these two structures is the presence of a small helix, B0, in spectrin repeat 5. Given that a later investigation found no such small helix in plectin (Ortega et al., 2016), we chose to model VAB-10 using 3R6N (desmoplakin), despite the fact that the sequence identity is lower (27.37% for desmoplakin as opposed to 32.10%). When compared to 3R6N, the obtained model has a distance of 0.46 Å between the 265 pairs of Cα atoms within 2.0 Å of each other out of a total of 274 pairs. As given by MODELLER's estimates, the homology model is at an RMSD of 2.21 Å and an overlap of Cα atoms of 0.91 within 3.5 Å. We compared the three structures (3PE0, 3R6N, and our obtained homology model) in Fig. 1E. We also obtained homology models for the

mutant protein VAB-10(mc64) lacking the first two helices of SR5, which show the SH3 domain still associated to helix 2C, but helix 3C is shown to loop back onto the rest of the structure in two different conformations (Fig. S3D).

Molecular dynamics simulations

We followed the same protocol as described in our previous work (Daday et al., 2017). In short, we used the Amber99SB-ILDN* force field (Liu et al., 2016) with a TIP3P water model (Jorgensen et al., 1983) and virtual sites(Berendsen and van Gunsteren, 1984), allowing for a 5 fs time step. All MD simulations were performed using GROMACS, version 5.0 (Pronk et al., 2013). We performed equilibrium molecular dynamics on approximately 190k atoms in a dodecahedron box for 1μs, and thereafter we chose the top 10 frames through cluster analysis between 100-1000 ns, with a cutoff of 0.088 nm. These 10 frames were later used for force-probe simulations. 10 simulations were performed at each of the velocities 1, 1/3, 1/10 nm/ns, and 3 simulations were performed at the velocity of 1/30 nm/ns. All other parameters were identical to the procedure described in our previous work, in particular for the re-solvation procedure for plectin. The equilibrium molecular dynamics simulation shows a backbone RMSD with an inter-quantile range between 3.4-4.4 Å. The helicity of the construct is very stable, with quartiles at 209 and 214 residues out of the 274 in our structure, and the β-strand content is stable, with quartiles at 35 and 40 residues and a small positive drift (1 more residue in strands every 236 ns). Overall, we consider the homology model to be a good representation of this region of VAB-10.

Image processing, quantification and statistical analysis

Images in Fig. 6 were analyzed as follows: the background was estimated by Gaussian filter of the original image with a width of 30 pixel; the background image was subtracted from the original one; the line profile of the GIT-1 signal along the hemidesmosomes was measured on the

subtracted image. We recorded two observables from the line profile: the average signal and its standard deviation. The average signal is shown in Fig. 6C, whereas the ratio between standard deviation and average signal (coefficient of variation) is shown in Fig. 6D as a measure of the discontinuity. Indeed a fragmented signal shows higher relative fluctuations. All images were analysed using the ImageJ (FiJi) software (NIH, Bethesda, Maryland, USA; http://rsb.info.nih.gov/ij/) and statistical test were performed using MATLAB R2018b (The MathWorks Inc., Natick, MA). For Fig. 6 a Wilcoxon test was used, whereas for Fig. 2H a chi-square test was applied.

Acknowledgements

We thank the *Caenorhabditis* Genetics Center (funded by the NIH Office of Research Infrastructure Programs P40 OD010440) for strains, and the IBPS Imaging Facility for advice. We thank also Thanh Vuong-Brender for critical reading of the manuscript. This work was supported by a European Research Council (grant #294744**)**, ANR (ANR-11-BSV2-0023) and installation funds from the Centre National de la Recherche Scientifique (CNRS) and University Pierre et Marie Curie (UPMC) to ML. This work was also made possible by institutional funds from the CNRS, University of Strasbourg and UPMC, the grant ANR-10-LABX-0030-INRT which is a French State fund managed by the Agence Nationale de la Recherche under the framework programme Investissements d'Avenir labelled ANR-10-IDEX-0002-02 to the IGBMC. FG acknowledges funding from the Klaus Tschira Foundation, from the German Research Foundation (DFG) through the priority programme SPP1782, and from the state of Baden-Württemberg and the DFG through grant INST 35/1134-1 FUGG.

Figure legends

Table 1. Phenotypes of mutations affecting the VAB-10 plakin domain

Figure 1. The SR4-SR5-SH3 domains of plectin and VAB-10 have a similar conformation

(A) Muscles are required for the embryo to elongate from the 2-fold stage (left) to the terminal 4-fold/prezel stage (right). **(A')** Cross-section of the embryo showing the relative positions of muscles and epidermal cells. **(B)** Comparison of the embryonic *C. elegans* and **(B')** vertebrate hemidesmosome junctions. The drawing is only showing essential *C. elegans* hemidesmosome proteins (GIT-1, PIX-1, PAK-1 not included). Besides intermediate filaments, the only conserved protein in common is the plakin: Plectin and BPAG1e in vertebrates, VAB-10A in *C. elegans* (green; the VAB-10B/MACF plakin transiently associates with the hemidesmosome). LET-805 basally, MUP-4 apically, the intermediate filament dimers IFA-3/ IFB-1, PAT-12 are nematode-specific proteins; VAB-19 and its binding partner EPS-8B have homologs in vertebrates (Kank1 and EPS8, respectively) which are not known to associate with vertebrate hemidesmosomes; the basal ECM ligand UNC-52 is homologous to perlecan, whereas the apical one includes several proteins with Zona Pellucida domains (Vuong-Brender et al., 2017; Zhang and Labouesse, 2010b). **(C)** Outline of the mechanotransduction pathway occurring in the epidermis in response to the tension created by the contraction of muscles, which are tightly linked to the epidermis. **(D)** Comparison of the plakin domain of plectin and spectraplakins, showing that all of them have a predicted SH3 domain nested within a spectrin domain. The structure prediction is based on (Choi and Weis, 2011; Daday et al., 2017; Ortega et al., 2016), and BLASTP alignments. Numbering of the SR domains is based on plectin in this and all subsequent figures (Ortega et al., 2011; Ortega et al., 2016). **(E)** 3D structure the SH3 and surrounding spectrin repeats from human Plectin (PDB 3PE0; blue), human desmoplakin (PDB 3RN6; green) and superimposed Pymol

prediction for the homologous spectrin repeat and SH3 domain from VAB-10 (orange). The only major difference between them is in the minor helix on the right.

Figure 2. The SR5 and SH3 domains of VAB-10 are important for embryonic elongation

(A) Position of the CRISPR-generated mutations in the plakin domain. **(B)** Alignment of the SH3 domain among spectraplakins and plakins (as predicted by the SMART software), along with the positions of the residues mutated by CRISPR. **(C-F')** DIC micrographs of an arrested *mc64* (noted Δ*SR5*) embryo (**C**), a *h1356* embryo which is a canonical *vab-10* null allele (**D**), a wild-type 2-fold embryo (**E'**) and young hatchling (**E'**), a rare malformed *mc62* (noted Δ*SH3*) young hatchling (**F**) and a more common *mc62* healthy sibling (**F'**). **(G)** Quantification of the embryonic and larval lethality rate among the main new *vab-10* alleles (see also Table1). **(H)** Allelic complementation tests between *mc55* or *mc62* and the very strong *vab-10A(ju281) and vab-10B(mc44)* alleles; the phenotypes correspond to those observed in the progeny of *mc62/ju281* and *mc62/mc44* trans-heterozygous adults. Chi-square analysis shows the distributions are not statistically different. **(I)** The VAB-10A and VAB-10B isoforms were tagged with mCherry and GFP, respectively. Additionally, these markers were introduced in a *vab-10(ΔSH3)* mutant, except that the GFP could not be obtained at the very C-term for *vab-10B(ΔSH3)*. Scale bars, 10 µm.

Figure 3. Strong synergistic interactions between novel *vab-10* alleles and mutations affecting the mechanotransduction pathway

(A) DIC pictures showing the elongation of control embryos (row 1), of *pak-1(RNAi)* embryos (row 2), *vab-10A(ΔSH3)* embryos (row 3), and *vab-10A(ΔSH3)* embryos after *pak-1(RNAi)* (row 4), *vab-10A(ΔSR8); pak-1(RNAi)* embryos (row 5), *vab-10A(ΔSH3); git-1(tm1962)* embryos (row 6), *vab-10A(ΔSH3); pak-1(ok448)* embryos (row 7); pictures from rows 2, 4 and 6 are Movies S1-S2-S3, respectively. The time interval between images is indicated at the top. Red arrow, localized

irregularity in the body wall. **(B)** Quantification of the embryonic and larval lethality in the double mutants shown in (**A**). **(C)** Elongation curves of the same double mutants. Scale bars, 10 µm.

Figure 4. The hemidesmosomes of *vab-10A(ΔSH3); pak-1(RNAi)* embryos collapse on the embryo convex side

(A-B) Spinning disc fluorescence micrographs from time-lapse movies of embryos with the genotypes indicated on the left; pictures were taken every 10 min and each panel represents the projection of approximately 15 focal planes (out of generally 60). **(A)** Embryos homozygous for the CRISPR knockin LET-805::GFP (*mc73*; top three rows; N=35) or the MUP-4::GFP knockin (*mc121*; bottom row; N=30). Note that in the *vab-10(ΔSH3); pak-1(RNAi)* embryo (3rd row), the LET-805::GFP signal has detached from the body wall on the convex side and collapsed internally (white arrows, area of detachment; white dotted line, body wall - compare to 1st and 2nd rows). Likewise, the MUP-4::GFP signal is much weaker on the convex side (between white arrows). Pictures in rows 2-3 are from Movies S4 and S5, respectively. All examined embryos showed a detachment. **(B)** Wild-type VAB-10(+)::mCherry; LET-805::GFP embryo alone or after *pak-1(RNAi)*; in both cases the 1st panel shows the GFP signal in the turn of the embryo, the 2nd the mCherry channel and the 3rd the merge channel at the 2.1/2.2-fold stage (row 1). Rows 2-4 show an embryo homozygous for *vab-10(mc62)::mCherry* and LET-805::GFP treated with *pak-1(RNAi)* at three different stages (last being 2.2-fold stage equivalent). This embryo displayed a small interruption in the hemidesmosome line visible at an earlier stage (arrow and line), which prefigured the area of detachment (white arrows); 20 out of 21 embryos showed detachment in the convex part, among which 7 had a detectable interruption. 2nd row, LET-805::GFP signal; 3rd row, VAB-10(mc62)::mCherry signal (the inset corresponds to a small area for which the intensity was increased with FiJi); 4th row, merge. Pictures in row 4 are from Movie S6. Scale bars, 10 µm.

Figure 5. VAB-10A and GIT-1 localize within less than 10 nm distance from each other.

(A) Spinning disc fluorescence images of 2-fold embryos homozygous for *vab-10A::mCherry* (*mc100*), *vab-10A(ΔSH3)::mCherry* (*mc109*), *vab-10B::GFP* (*mc123*), or *vab-10B(ΔSH3)::GFP* (*mc124*). The pattern of VAB-10A and VAB-10B was identical to that observed with antibodies (Bosher et al., 2003), and remained unaffected by the *ΔSH3* deletion. (**B**) Spinning disc fluorescence images of a 2-fold embryo homozygous for the CRISPR-generated knockin *git-1::GFP* (*mc86*). **(C)** Strategy for the bi-fluorescence complementation strategy to define whether VAB-10A and GIT-1 are in close proximity. VEN, fusion with residues 1-173 of the Venus protein; US, fusion with residues 155-238 of the Venus protein. **(D)** Wide-field (upper panels) and spinning disc fluorescence (lower panels) micrographs of embryos expressing PIX-1::Venus(155-238), GIT-1::Venus(1-173), VAB-10A::Venus(155-238), GIT-1::Venus(1-173) with PIX-1::Venus(155-238), GIT-1::Venus(1-173) with VAB-10A::Venus(155-238). Note the clear hemidesmosomal pattern in the last two panels (arrows). Scale bars, 10 µm.

Figure 6. Differential requirement of hemidesmosome components for GIT-1 recruitment

(A) Spinning disc fluorescence pictures from movies S7-S12 showing the distribution of the GIT-1::GFP knockin (allele *mc86*) at the 1.5-fold stage and 10, 20 and 60 minutes later for the genetic backgrounds indicated on the left. Each picture shows only the top two hemidesmosomes. Note how the hemidesmosome signal is collapsing internally from the most convex side of the embryo for *pat-12*, *vab-10* and *let-805* knockout embryos as well as for *vab-10(ΔSR5h1-h2)* embryos (arrows). **(B-B')** Procedure used for image analysis to quantify the signal intensity and continuity: after background subtraction (**B**), the signal intensity was measured along the hemidesmosome signal between the two arrows. (**B'**) Examples of the signal for two backgrounds, but just for the area bracketed by short horizontal white lines in (**B**). **(C-D)** Signal intensity (**C**) and continuity (**D**) for the backgrounds illustrated in (**A**) at three time points. Scale bar, 10 µm. Statistical tests: ns, not significant; *, $p < 0.5$; **, $p < 0.01$; ***, $p < 0.001$.

Figure 7. Unfolding forces exerted on the plakin domain of VAB-10 unmask the SH3 domain

(A) Mechanical unfolding pathways of VAB-10 and plectin lead to SH3 activation. The numbers indicate how many trajectories showed SR4 unfolding first (left) versus SR5 unfolding first (right). Numbers for plectin are based on (Daday et al., 2017). Red, SR4; green, SR5 (the thickness of the green rectangle is proportional to the number of helices contributing to it); blue, SH3-SR4 interface; grey: SH3, star: exposure; wavy red/green lines, unfolded SR helices. **(B)** Model for mechanosensing at the hemidesmosome (see text).

Figure S1. Genetic interactions between the *pak-1* and *vab-10(ΔSR7)* or *vab-10(ΔSR8)* deletions

(A) DIC micrographs taken from time-lapse movies of wild-type (1st row), *vab-10(ΔSH3); pix-1(gk416)* (2nd row), *vab-10(ΔSH3); pak-1(RNAi)* (3rd row), *vab-10(ΔSR7); pak-1(RNAi)* (4th row). **(B)** Homozygous *vab-10(ΔSR7)* (1st row) and *vab-10(ΔSR8)* (2nd row) carrying the LET-805::GFP (*mc73*) after RNAi against *pak-1*. Note that hemidesmosomes collapsed in the turn of the *vab-10(ΔSR8)* embryo. Scale bars, 10 µm.

Figure S2. Hemidesmosome defects trigger muscle detachment

Fluorescence pictures taken from a video from homozygous *vab-10(ΔSH3)::mCherry* carrying a transgene expressing specifically a cytoplasmic GFP in muscles (marker HBR4). Genotypes are indicated above each series. Muscles detach from the outer body wall in *vab-10(ΔSH3); pak-1(RNAi)* embryos (arrows). Scale bar, 10 µm.

Figure S3. Embryos lacking the first half of the SR5 express LET-805::GFP

Fluorescence pictures taken from a video from homozygous *vab-10(ΔSR5h1-h2); let-805::gfp*. Note that although hemidesmosomes are collapsing (arrows), the GFP level remains very high by contrast to what is reported in Fig. 4 for *vab-10(ΔSH3); pak-1(RNAi)* embryos. Scale bar, 10 µm.

Figure S4. Quantification of the molecular dynamics simulations for VAB-10A plakin domain Molecular dynamics simulation data on which Fig. 7 is based. **(A)** Points of SH3 activation and SH3 unfolding as a function of total extension (vt), depending on the pulling velocity. In all simulations, the activation and unfolding are decoupled events and activation happens first. **(B)** The frequency of the active extension of VAB10. For example, 30 nm means that after SH3 domain activation, another 30 nm of extension is required for the SH3 domain to start unfolding. **(C)** Comparison of rupture forces between plectin, desmoplakin and VAB-10. Note that VAB-10 appears to show an intermediate rupture force between plectin and desmoplakin. **(D)** Predicted 3D structure of the SR4-SR(+SH3)5 domain of VAB-10 (grey), and that of the same area for the mutant VAB-10(mc64) protein lacking the first two helices of SR5. The prediction is that the SH3 domain could still bind to SR4, but that most likely the remaining helix3 of SR5 would be destabilized (shown in two orientations).

Captions for movies

Movie S1: DIC time-lapse video of a *pak-1(RNAi)* embryo during its active elongation.

Movie S2: DIC time-lapse video of a *vab-10(ΔSH3); pak-1(RNAi)* embryo during elongation.

Movie S3: DIC time-lapse video of a *vab-10(ΔSH3); git-1(tm1962)* embryo during elongation.

Movie S4: Fluorescence time-lapse video of a *pak-1(RNAi)* embryo homozygous for *let-805::gfp* during elongation.

Movie S5: Fluorescence time-lapse video of a *vab-10(ΔSH3); pak-1(RNAi)* embryo homozygous for *let-805::gfp* during elongation.

Movie S6: Fluorescence time-lapse video of a *vab-10(ΔSH3)::mCherry; pak-1(RNAi)* embryo homozygous for *let-805::gfp* during elongation.

Movie S7: Combined fluorescence video of embryos homozygous for *git-1::gfp* after knocking down the genes indicated on the movie.

Movies S1-S3 correspond to a single focal plane, Movies S4-S7 to the full projection. The frame rate is 30 frames/second (Movies S1-S3), 15 frames/second (Movies S4-S6) and 6 frames/second (Movie S7).

References

Almeida, F.V., G. Walko, J.R. McMillan, J.A. McGrath, G. Wiche, A.H. Barber, and J.T. Connelly. 2015. The cytolinker plectin regulates nuclear mechanotransduction in keratinocytes. *J Cell Sci*. 128:4475-4486.

Berendsen, H.J.C., and W.F. van Gunsteren. 1984. Molecular dynamics simulations: techniques and approaches. *In* On molecular liquids — dynamics and interactions. Vol. C135. A.J. Barnes, W.J. Orville-Thomas, and J. Yarwood, editors. NATO ASI Series,, Reidel, Dordrecht. 475-500.

Bosher, J.M., B.S. Hahn, R. Legouis, S. Sookhareea, R.M. Weimer, A. Gansmuller, A.D. Chisholm, A.M. Rose, J.L. Bessereau, and M. Labouesse. 2003. The *Caenorhabditis elegans vab-10* spectraplakin isoforms protect the epidermis against internal and external forces. *J Cell Biol*. 161:757-768.

Chen, Y., L. Ju, M. Rushdi, C. Ge, and C. Zhu. 2017. Receptor-mediated cell mechanosensing. *Mol Biol Cell*. 28:3134-3155.

Choi, H.J., and W.I. Weis. 2011. Crystal structure of a rigid four-spectrin-repeat fragment of the human desmoplakin plakin domain. *J Mol Biol*. 409:800-812.

Ciruela, F., J.P. Vilardaga, and V. Fernandez-Duenas. 2010. Lighting up multiprotein complexes: lessons from GPCR oligomerization. *Trends Biotechnol*. 28:407-415.

Daday, C., K. Kolsek, and F. Grater. 2017. The mechano-sensing role of the unique SH3 insertion in plakin domains revealed by Molecular Dynamics simulations. *Sci Rep*. 7:11669.

del Rio, A., R. Perez-Jimenez, R. Liu, P. Roca-Cusachs, J.M. Fernandez, and M.P. Sheetz. 2009. Stretching single talin rod molecules activates vinculin binding. *Science*. 323:638-641.

Dickinson, D.J., J.D. Ward, D.J. Reiner, and B. Goldstein. 2013. Engineering the Caenorhabditis elegans genome using Cas9-triggered homologous recombination. *Nat Methods*. 10:1028-1034.

Francis, R., and R.H. Waterston. 1991. Muscle cell attachment in Caenorhabditis elegans. *J Cell Biol*. 114:465-479.

Frank, S.R., and S.H. Hansen. 2008. The PIX-GIT complex: a G protein signaling cassette in control of cell shape. *Semin Cell Dev Biol*. 19:234-244.

Frijns, E., I. Kuikman, S. Litjens, M. Raspe, K. Jalink, M. Ports, K. Wilhelmsen, and A. Sonnenberg. 2012. Phosphorylation of threonine 1736 in the C-terminal tail of integrin beta4 contributes to hemidesmosome disassembly. *Mol Biol Cell*. 23:1475-1485.

Gieseler, K., H. Qadota, and G.M. Benian. 2017. Development, structure, and maintenance of C. elegans body wall muscle. *WormBook*. 2017:1-59.

Gilmour, D., M. Rembold, and M. Leptin. 2017. From morphogen to morphogenesis and back. *Nature*. 541:311-320.

Haining, A.W.M., R. Rahikainen, E. Cortes, D. Lachowski, A. Rice, M. von Essen, V.P. Hytonen, and A. Del Rio Hernandez. 2018. Mechanotransduction in talin through the interaction of the R8 domain with DLC1. *PLoS Biol*. 16:e2005599.

Hresko, M.C., L.A. Schriefer, P. Shrimankar, and R.H. Waterston. 1999. Myotactin, a novel hypodermal protein involved in muscle-cell adhesion in *Caenorhabditis elegans*. *J Cell Biol*. 146:659-672.

Hu, C.D., Y. Chinenov, and T.K. Kerppola. 2002. Visualization of interactions among bZIP and Rel family proteins in living cells using bimolecular fluorescence complementation. *Mol Cell*. 9:789-798.

Hu, X., F.M. Margadant, M. Yao, and M.P. Sheetz. 2017. Molecular stretching modulates mechanosensing pathways. *Protein Sci*. 26:1337-1351.

Iskratsch, T., H. Wolfenson, and M.P. Sheetz. 2014. Appreciating force and shape-the rise of mechanotransduction in cell biology. *Nat Rev Mol Cell Biol*. 15:825-833.

Jorgensen, W.L., J. Chandrasekhar, and J.D. Madura. 1983. Comparison of simple potential functions for simulating liquid water *CJ Chem Phys*. 79:926-935.

Koster, J., S. van Wilpe, I. Kuikman, S.H. Litjens, and A. Sonnenberg. 2004. Role of binding of plectin to the integrin beta4 subunit in the assembly of hemidesmosomes. *Mol Biol Cell*. 15:1211-1223.

Ladoux, B., W.J. Nelson, J. Yan, and R.M. Mege. 2015. The mechanotransduction machinery at work at adherens junctions. *Integr Biol (Camb)*. 7:1109-1119.

Law, R., P. Carl, S. Harper, P. Dalhaimer, D.W. Speicher, and D.E. Discher. 2003. Cooperativity in forced unfolding of tandem spectrin repeats. *Biophys J*. 84:533-544.

le Duc, Q., Q. Shi, I. Blonk, A. Sonnenberg, N. Wang, D. Leckband, and J. de Rooij. 2010. Vinculin potentiates E-cadherin mechanosensing and is recruited to actin-anchored sites within adherens junctions in a myosin II-dependent manner. *J Cell Biol*. 189:1107-1115.

Lenne, P.F., A.J. Raae, S.M. Altmann, M. Saraste, and J.K. Horber. 2000. States and transitions during forced unfolding of a single spectrin repeat. *FEBS Lett*. 476:124-128.

Liu, A.S., H. Wang, C.R. Copeland, C.S. Chen, V.B. Shenoy, and D.H. Reich. 2016. Matrix viscoplasticity and its shielding by active mechanics in microtissue models: experiments and mathematical modeling. *Sci Rep*. 6:33919.

Moore, S.W., P. Roca-Cusachs, and M.P. Sheetz. 2010. Stretchy proteins on stretchy substrates: the important elements of integrin-mediated rigidity sensing. *Dev Cell*. 19:194-206.

Ortega, E., R.M. Buey, A. Sonnenberg, and J.M. de Pereda. 2011. The structure of the plakin domain of plectin reveals a non-canonical SH3 domain interacting with its fourth spectrin repeat. *J Biol Chem*. 286:12429-12438.

Ortega, E., J.A. Manso, R.M. Buey, A.M. Carballido, A. Carabias, A. Sonnenberg, and J.M. de Pereda. 2016. The Structure of the Plakin Domain of Plectin Reveals an Extended Rod-like Shape. *J Biol Chem*. 291:18643-18662.

Pettersen, E.F., T.D. Goddard, C.C. Huang, G.S. Couch, D.M. Greenblatt, E.C. Meng, and T.E. Ferrin. 2004. UCSF Chimera--a visualization system for exploratory research and analysis. *J Comput Chem*. 25:1605-1612.

Pronk, S., S. Pall, R. Schulz, P. Larsson, P. Bjelkmar, R. Apostolov, M.R. Shirts, J.C. Smith, P.M. Kasson, D. van der Spoel, B. Hess, and E. Lindahl. 2013. GROMACS 4.5: a high-throughput and highly parallel open source molecular simulation toolkit. *Bioinformatics*. 29:845-854.

Sali, A., and T.L. Blundell. 1993. Comparative protein modelling by satisfaction of spatial restraints. *J Mol Biol*. 234:779-815.

Sawada, Y., and M.P. Sheetz. 2002. Force transduction by Triton cytoskeletons. *J Cell Biol*. 156:609-615.

Sawada, Y., M. Tamada, B.J. Dubin-Thaler, O. Cherniavskaya, R. Sakai, S. Tanaka, and M.P. Sheetz. 2006. Force sensing by mechanical extension of the Src family kinase substrate p130Cas. *Cell*. 127:1015-1026.

Takawira, D., G.R. Budinger, S.B. Hopkinson, and J.C. Jones. 2011. A dystroglycan/plectin scaffold mediates mechanical pathway bifurcation in lung epithelial cells. *J Biol Chem*. 286:6301-6310.

Valencia, R.G., G. Walko, L. Janda, J. Novacek, E. Mihailovska, S. Reipert, K. Andra-Marobela, and G. Wiche. 2013. Intermediate filament-associated cytolinker plectin 1c destabilizes microtubules in keratinocytes. *Mol Biol Cell*. 24:768-784.

Vuong-Brender, T.T., X. Yang, and M. Labouesse. 2016. C. elegans Embryonic Morphogenesis. *Curr Top Dev Biol*. 116:597-616.

Vuong-Brender, T.T.K., S.K. Suman, and M. Labouesse. 2017. The apical ECM preserves embryonic integrity and distributes mechanical stress during morphogenesis. *Development*.

Yao, M., B.T. Goult, B. Klapholz, X. Hu, C.P. Toseland, Y. Guo, P. Cong, M.P. Sheetz, and J. Yan. 2016. The mechanical response of talin. *Nat Commun*. 7:11966.

Yao, M., W. Qiu, R. Liu, A.K. Efremov, P. Cong, R. Seddiki, M. Payre, C.T. Lim, B. Ladoux, R.M. Mege, and J. Yan. 2014. Force-dependent conformational switch of alpha-catenin controls vinculin binding. *Nat Commun*. 5:4525.

Yonemura, S., Y. Wada, T. Watanabe, A. Nagafuchi, and M. Shibata. 2010. alpha-Catenin as a tension transducer that induces adherens junction development. *Nat Cell Biol*. 12:533-542.

Zahreddine, H., H. Zhang, M. Diogon, Y. Nagamatsu, and M. Labouesse. 2010. CRT-1/calreticulin and the E3 ligase EEL-1/HUWE1 control hemidesmosome maturation in *C. elegans* development. *Curr Biol*. 20:322-327.

Zhang, H., and M. Labouesse. 2010a. The making of hemidesmosome structures in vivo. *Dev Dyn*. 239:1465-1476.

Zhang, H., and M. Labouesse. 2010b. The making of hemidesmosome structures in vivo. *Developmental Dynamics*. 239:1465-1476.

Zhang, H., F. Landmann, H. Zahreddine, D. Rodriguez, M. Koch, and M. Labouesse. 2011. A tension-induced mechanotransduction pathway promotes epithelial morphogenesis. *Nature*. 471:99–103.

Zhang, J., J. Yue, and X. Wu. 2017. Spectraplakin family proteins - cytoskeletal crosslinkers with versatile roles. *J Cell Sci*. 130:2447-2457.

Figure 1

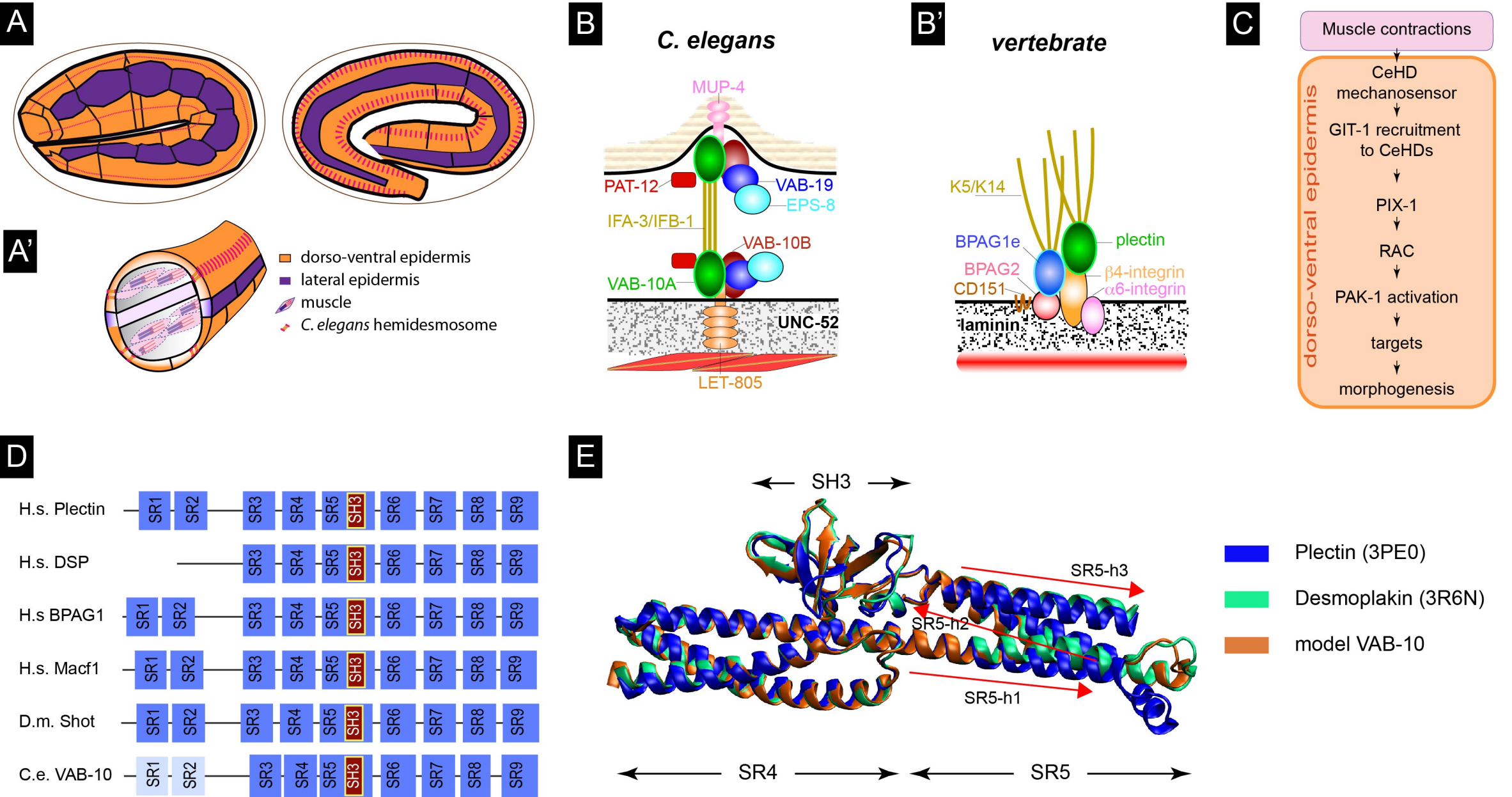
A
A'
dorso-ventral epidermis
lateral epidermis
muscle
C. elegans hemidesmosome
B
C. elegans
MUP-4
PAT-12
VAB-19
EPS-8
IFA-3/IFB-1
VAB-10B
VAB-10A
UNC-52
LET-805
B'
vertebrate
K5/K14
BPAG1e
plectin
BPAG2
β4-integrin
CD151
α6-integrin
laminin
C
Muscle contractions
CeHD mechanosensor
GIT-1 recruitment to CeHDs
PIX-1
RAC
PAK-1 activation
targets
morphogenesis
dorso-ventral epidermis
D
H.s. Plectin
H.s. DSP
H.s BPAG1
H.s. Macf1
D.m. Shot
C.e. VAB-10
SR1
SR2
SR3
SR4
SR5
SH3
SR6
SR7
SR8
SR9
E
SH3
SR5-h3
SR5-h2
SR5-h1
SR4
SR5
Plectin (3PE0)
Desmoplakin (3R6N)
model VAB-10

Figure 2

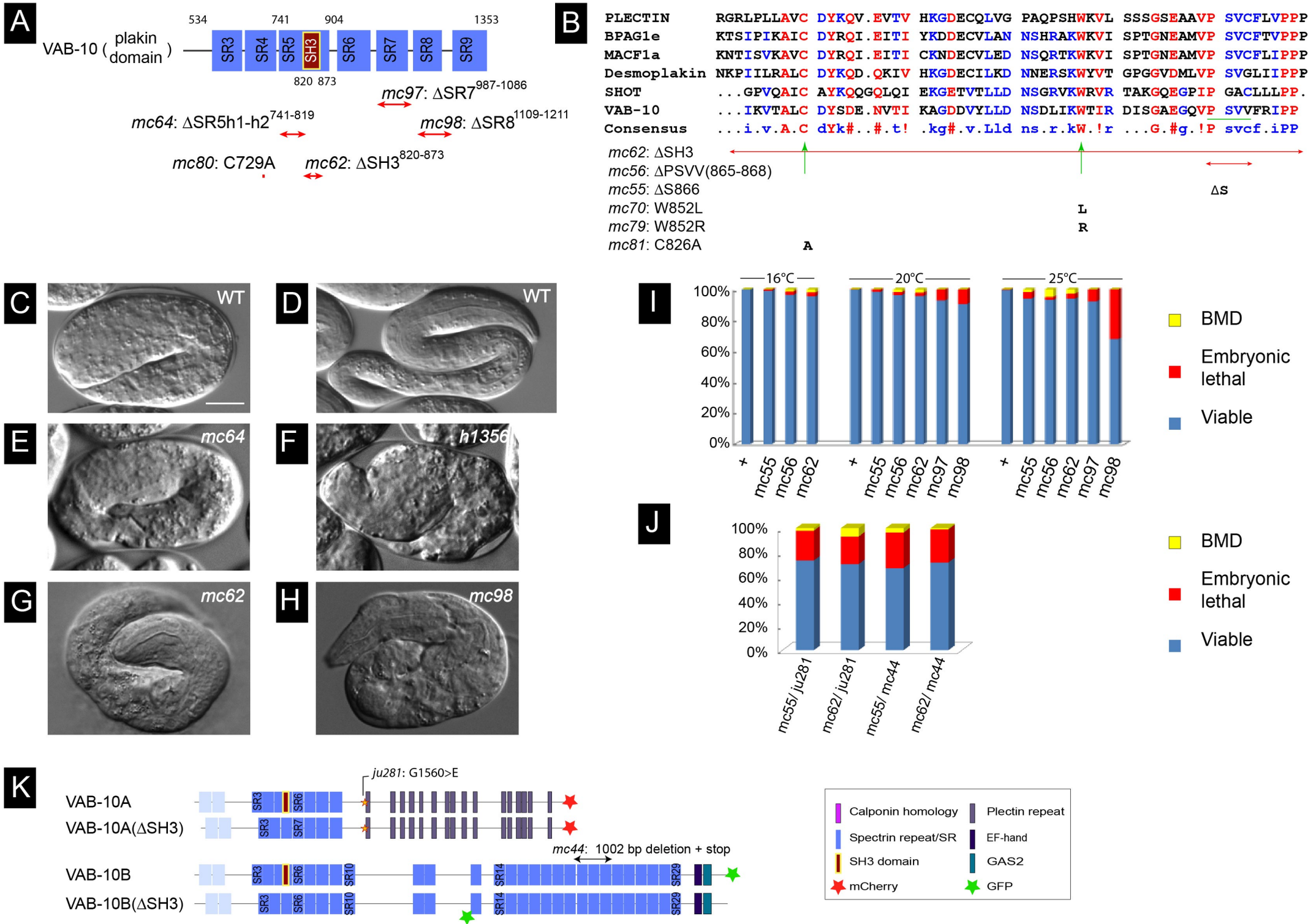
A
VAB-10 (plakin domain)
534
741
904
1353
SR3
SR4
SR5
SH3
SR6
SR7
SR8
SR9
820 873
mc97: ΔSR7 987-1086
mc64: ΔSR5h1-h2 741-819
mc98: ΔSR8 1109-1211
mc80: C729A
mc62: ΔSH3 820-873
B
PLECTIN RGRLPLLAVC DYKQV.EVTV HKGDECQLVG PAQPSHWKVL SSSGSEAAVP SVCFLVPPP
BPAG1e KTSIPIKAIC DYRQI.EITI YKDDECVLAN NSHRAKWKVI SPTGNEAMVP SVCFTVPPP
MACF1a KNTISVKAVC DYRQI.EITI CKNDECVLED NSQRTKWKVI SPTGNEAMVP SVCFLIPPP
Desmoplakin NKPIILRALC DYKQD.QKIV HKGDECILKD NNERSKWYVT GPGGVDMLVP SVGLIIPPP
SHOT ...GPVQAIC AYKQQGQLQI EKGETVTLLD NSGRVKWRVR TAKGQEGPIP GACLLLPP.
VAB-10 ...IKVTALC DYSDE.NVTI KAGDDVYLLD NSDLIKWTIR DISGAEGQVP SVVFRIPP
Consensus ...i.v.A.C dYk#..#.t! .kg#.v.Lld ns.r.kW.!r ...G.#g.!P svcf.iPP
mc62: ΔSH3
mc56: ΔPSVV(865-868)
mc55: ΔS866
mc70: W852L
mc79: W852R
mc81: C826A
A
L
R
ΔS
C
WT
D
WT
E
mc64
F
h1356
G
mc62
H
mc98
I
16°C
20°C
25°C
100%
80%
60%
40%
20%
0%
+
mc55
mc56
mc62
mc97
mc98
BMD
Embryonic lethal
Viable
J
100%
80%
60%
40%
20%
0%
mc55/ ju281
mc62/ ju281
mc55/ mc44
mc62/ mc44
BMD
Embryonic lethal
Viable
K
ju281: G1560>E
VAB-10A
VAB-10A(ΔSH3)
mc44: 1002 bp deletion + stop
VAB-10B
VAB-10B(ΔSH3)
SR3
SR6
SR7
SR10
SR14
SR29
Calponin homology
Spectrin repeat/SR
SH3 domain
mCherry
Plectin repeat
EF-hand
GAS2
GFP

Figure 3

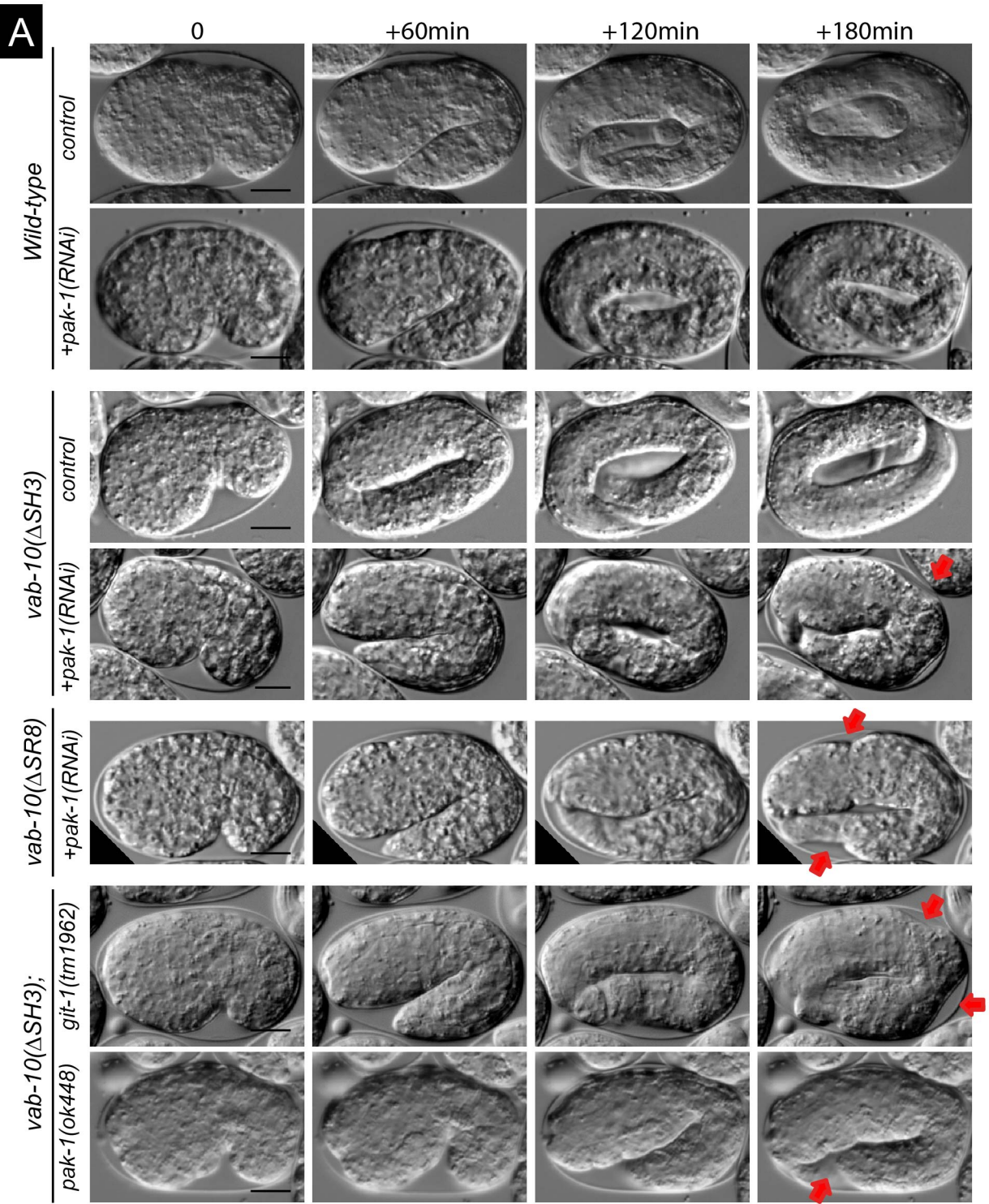
A
0
+60min
+120min
+180min
Wild-type
control
+pak-1(RNAi)
vab-10(ΔSH3)
control
+pak-1(RNAi)
vab-10(ΔSR8)
+pak-1(RNAi)
vab-10(ΔSH3);
git-1(tm1962)
pak-1(ok448)

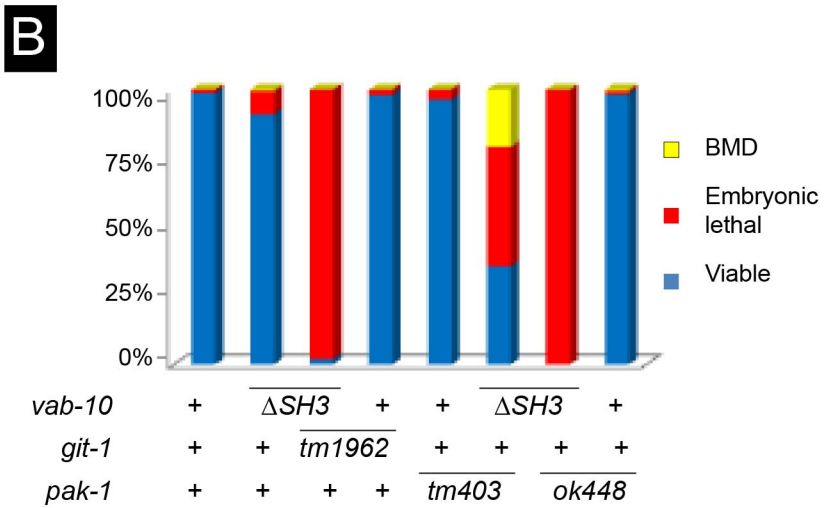
B
100%
75%
50%
25%
0%
BMD
Embryonic lethal
Viable
vab-10 + ΔSH3 + + ΔSH3 +
git-1 + + tm1962 + + + +
pak-1 + + + + tm403 ok448

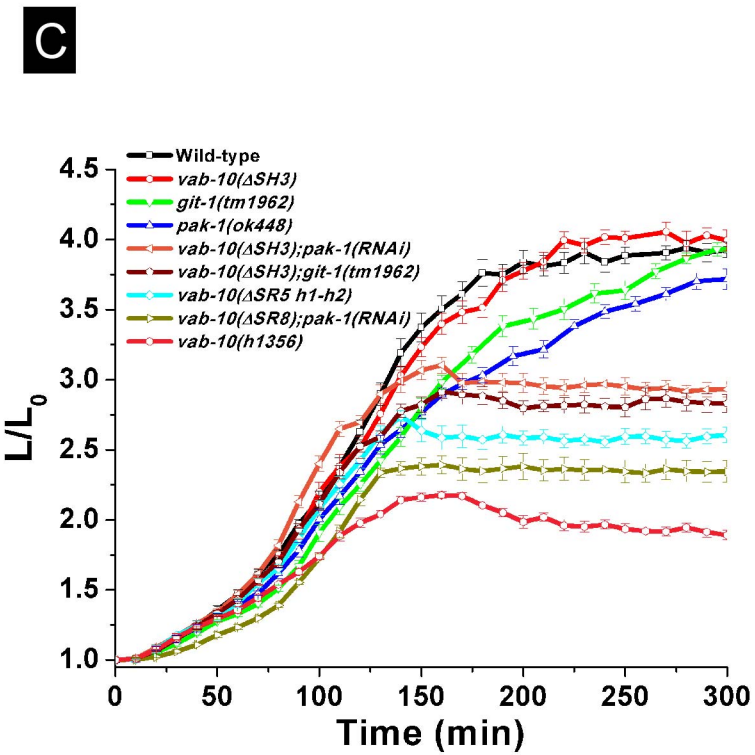
C
Wild-type
vab-10(ΔSH3)
git-1(tm1962)
pak-1(ok448)
vab-10(ΔSH3);pak-1(RNAi)
vab-10(ΔSH3);git-1(tm1962)
vab-10(ΔSR5 h1-h2)
vab-10(ΔSR8);pak-1(RNAi)
vab-10(h1356)
L/L0
4.5
4.0
3.5
3.0
2.5
2.0
1.5
1.0
0
50
100
150
200
250
300
Time (min)

Figure 4

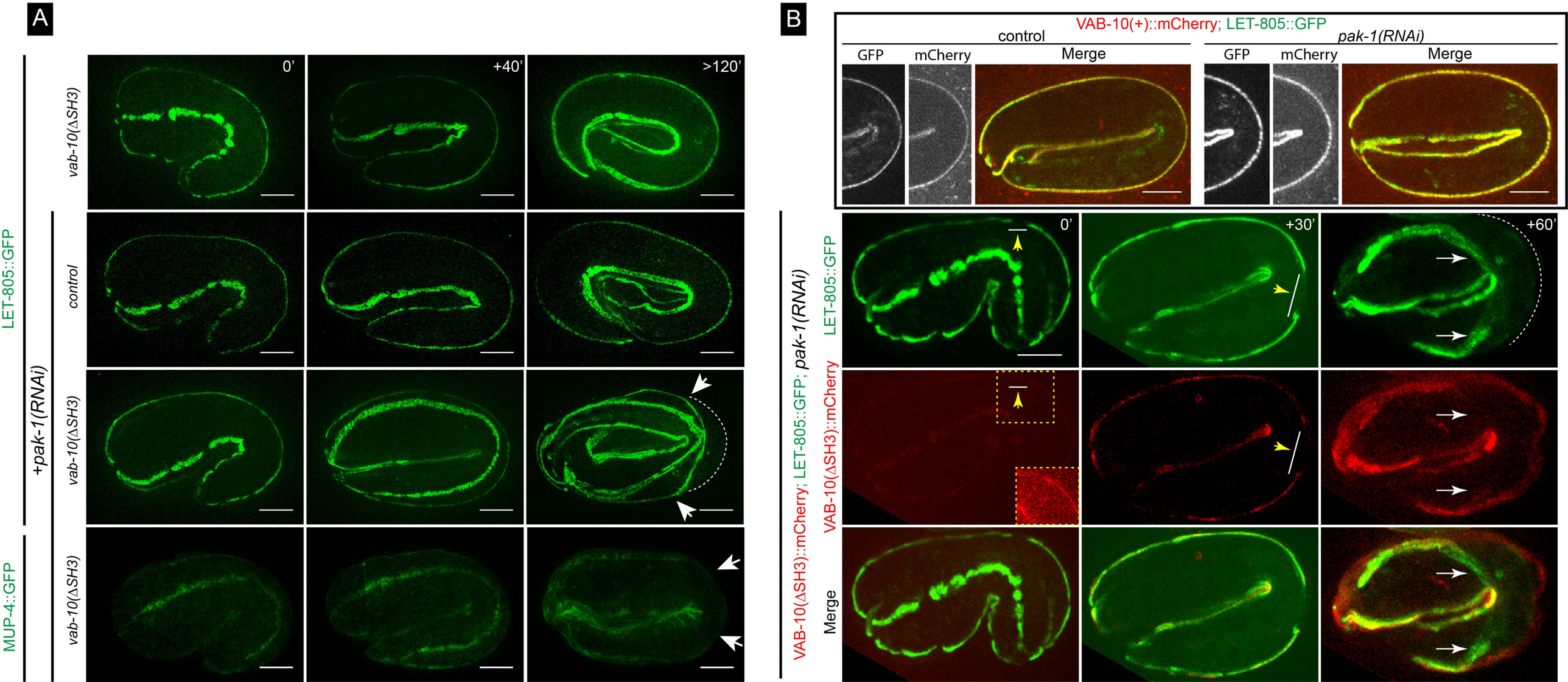
A
LET-805::GFP
MUP-4::GFP
+pak-1(RNAi)
vab-10(ΔSH3)
control
vab-10(ΔSH3)
vab-10(ΔSH3)
0'
+40'
>120'
B
VAB-10(+)::mCherry; LET-805::GFP
control
pak-1(RNAi)
GFP
mCherry
Merge
GFP
mCherry
Merge
VAB-10(ΔSH3)::mCherry; LET-805::GFP; pak-1(RNAi)
LET-805::GFP
VAB-10(ΔSH3)::mCherry
Merge
0'
+30'
+60'

Figure 5

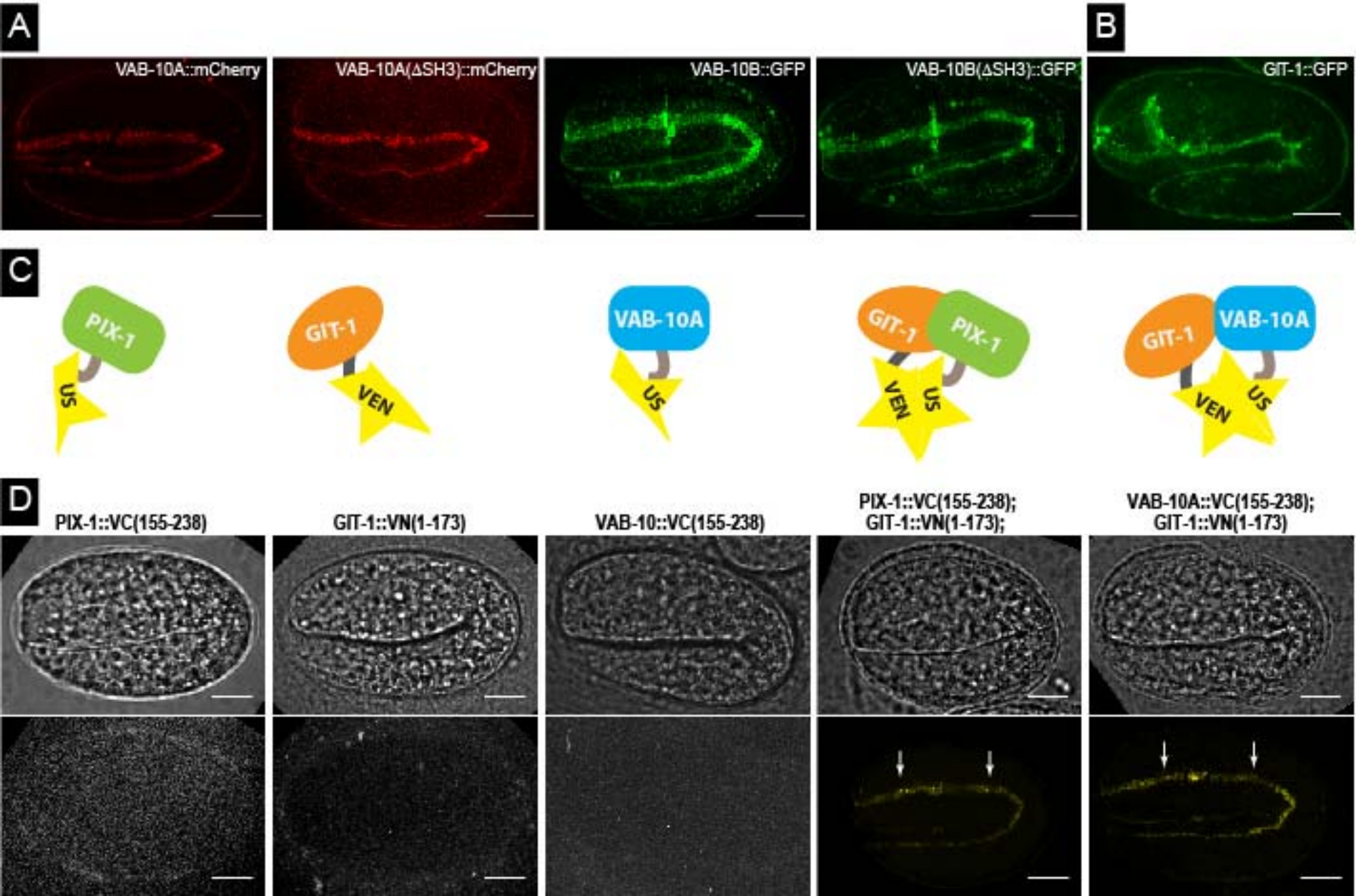
A
VAB-10A::mCherry
VAB-10A(ΔSH3)::mCherry
VAB-10B::GFP
VAB-10B(ΔSH3)::GFP
B
GIT-1::GFP
C
PIX-1
US
GIT-1
VEN
VAB-10A
US
GIT-1
PIX-1
VEN
US
GIT-1
VAB-10A
VEN
US
D
PIX-1::VC(155-238)
GIT-1::VN(1-173)
VAB-10::VC(155-238)
PIX-1::VC(155-238);
GIT-1::VN(1-173);
VAB-10A::VC(155-238);
GIT-1::VN(1-173)

Figure 6

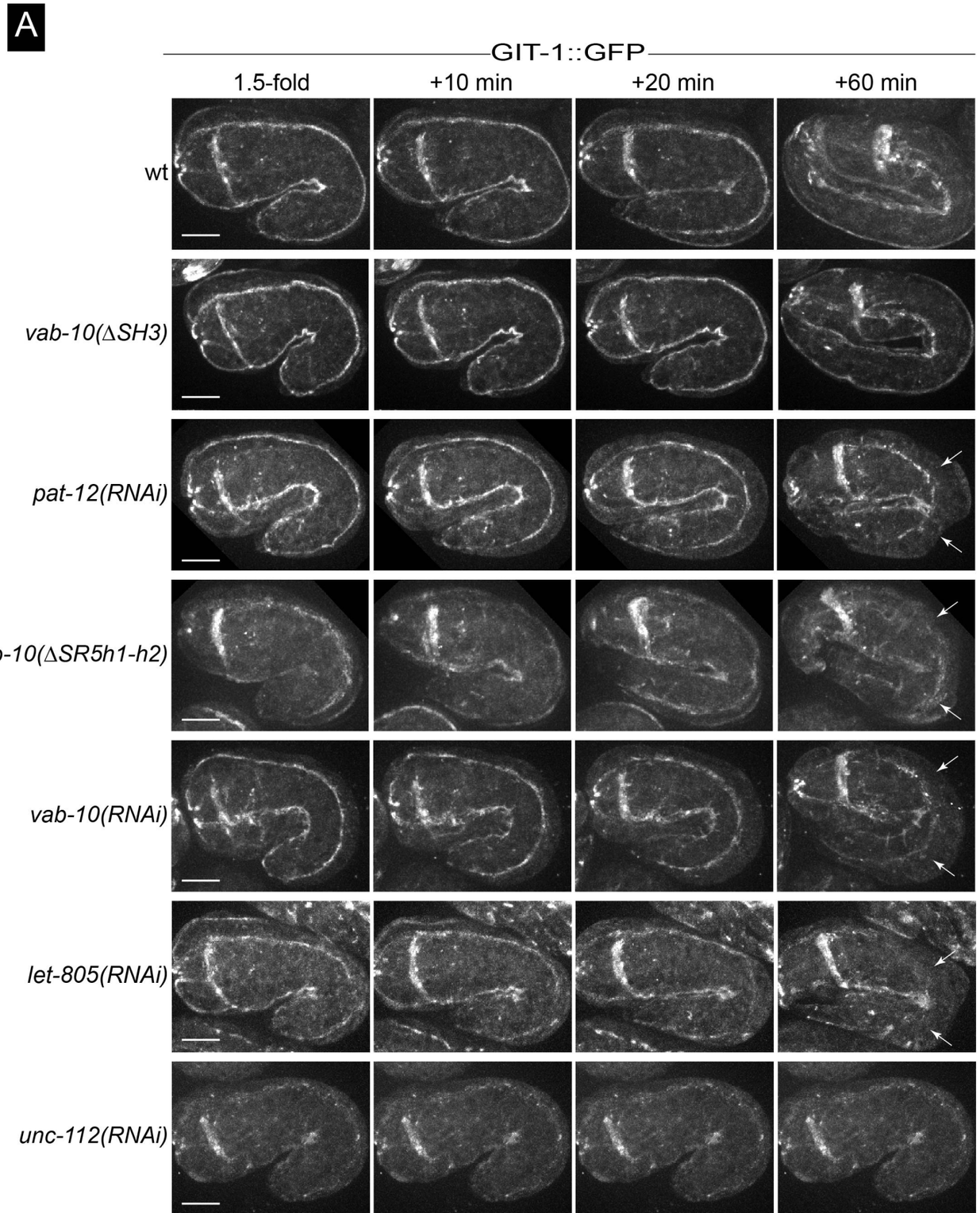
A
GIT-1::GFP
1.5-fold
+10 min
+20 min
+60 min
wt
vab-10(ΔSH3)
pat-12(RNAi)
vab-10(ΔSR5h1-h2)
vab-10(RNAi)
let-805(RNAi)
unc-112(RNAi)

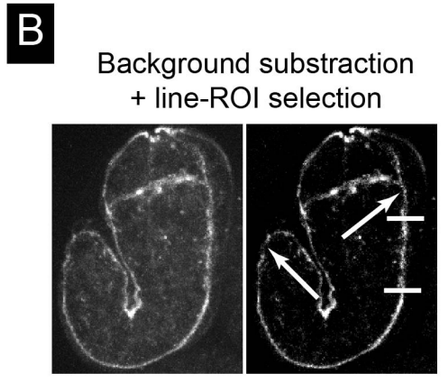
B
Background substraction
+ line-ROI selection

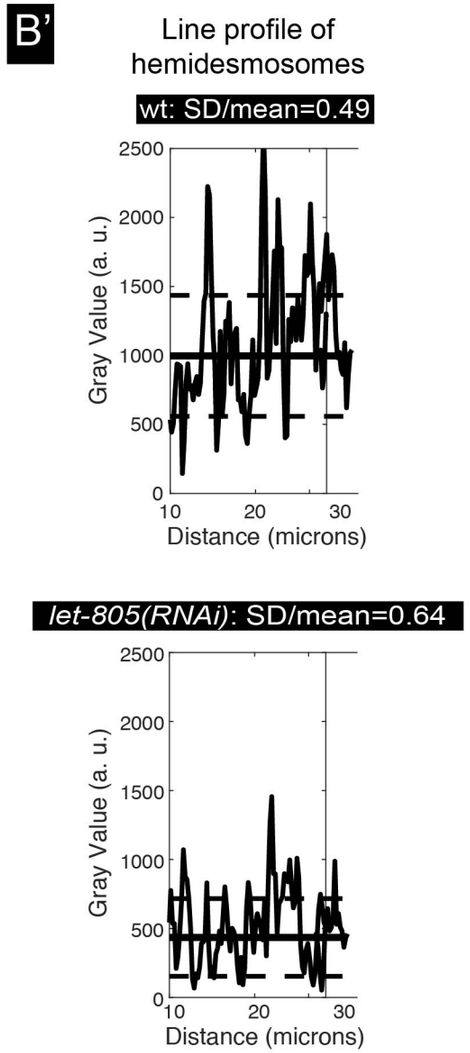
B'
Line profile of
hemidesmosomes
wt: SD/mean=0.49
let-805(RNAi): SD/mean=0.64
Gray Value (a. u.)
Distance (microns)

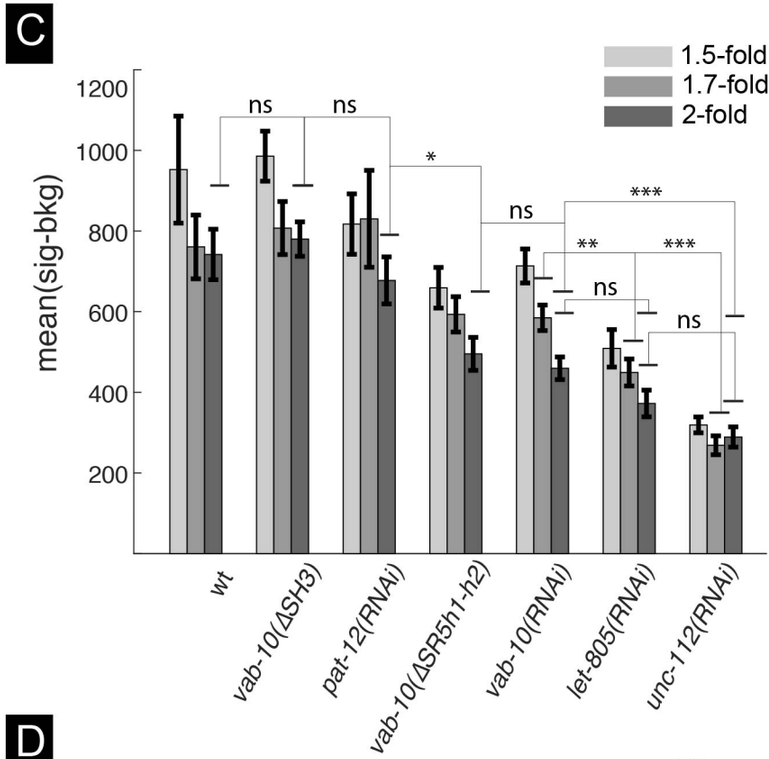
C
1.5-fold
1.7-fold
2-fold
mean(sig-bkg)
ns
*
**
***
wt
vab-10(ΔSH3)
pat-12(RNAi)
vab-10(ΔSR5h1-h2)
vab-10(RNAi)
let-805(RNAi)
unc-112(RNAi)

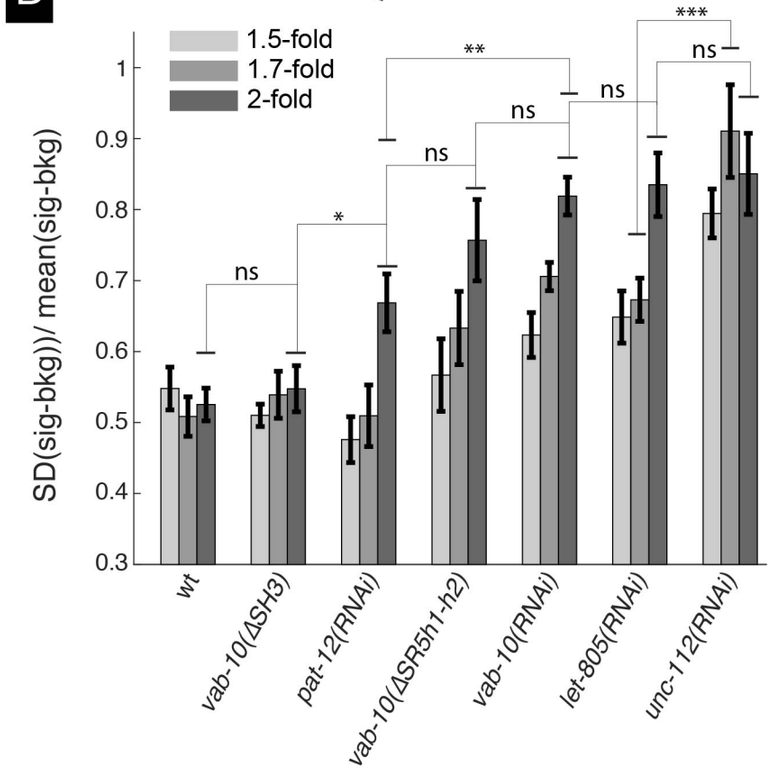
D
1.5-fold
1.7-fold
2-fold
SD(sig-bkg))/ mean(sig-bkg)
ns
*
**
***
wt
vab-10(ΔSH3)
pat-12(RNAi)
vab-10(ΔSR5h1-h2)
vab-10(RNAi)
let-805(RNAi)
unc-112(RNAi)

Figure 7

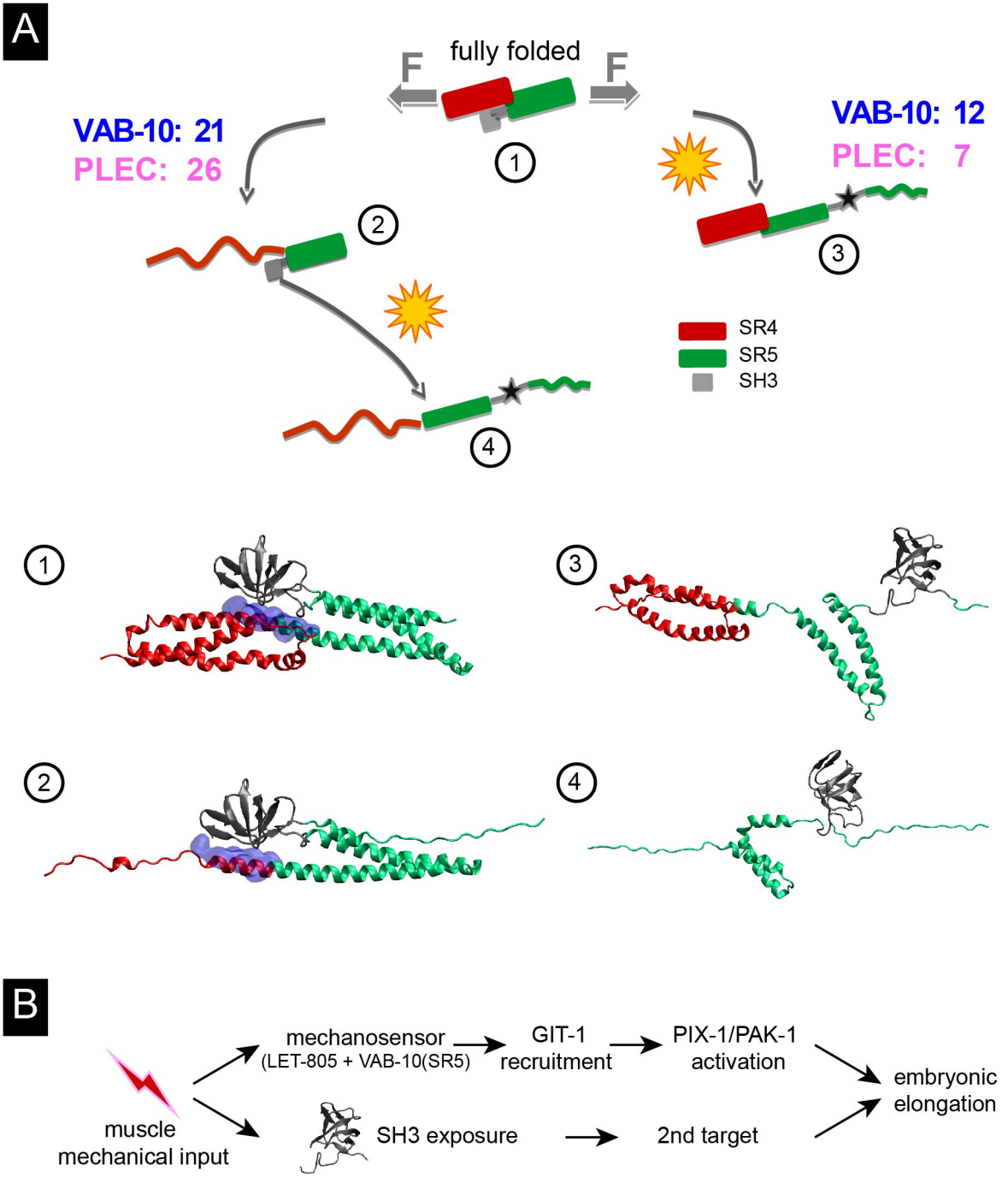
A
fully folded
F
F
VAB-10: 21
PLEC: 26
VAB-10: 12
PLEC: 7
1
2
3
4
SR4
SR5
SH3
B
muscle
mechanical input
mechanosensor
(LET-805 + VAB-10(SR5)
GIT-1
recruitment
PIX-1/PAK-1
activation
SH3 exposure
2nd target
embryonic
elongation

Figure S1

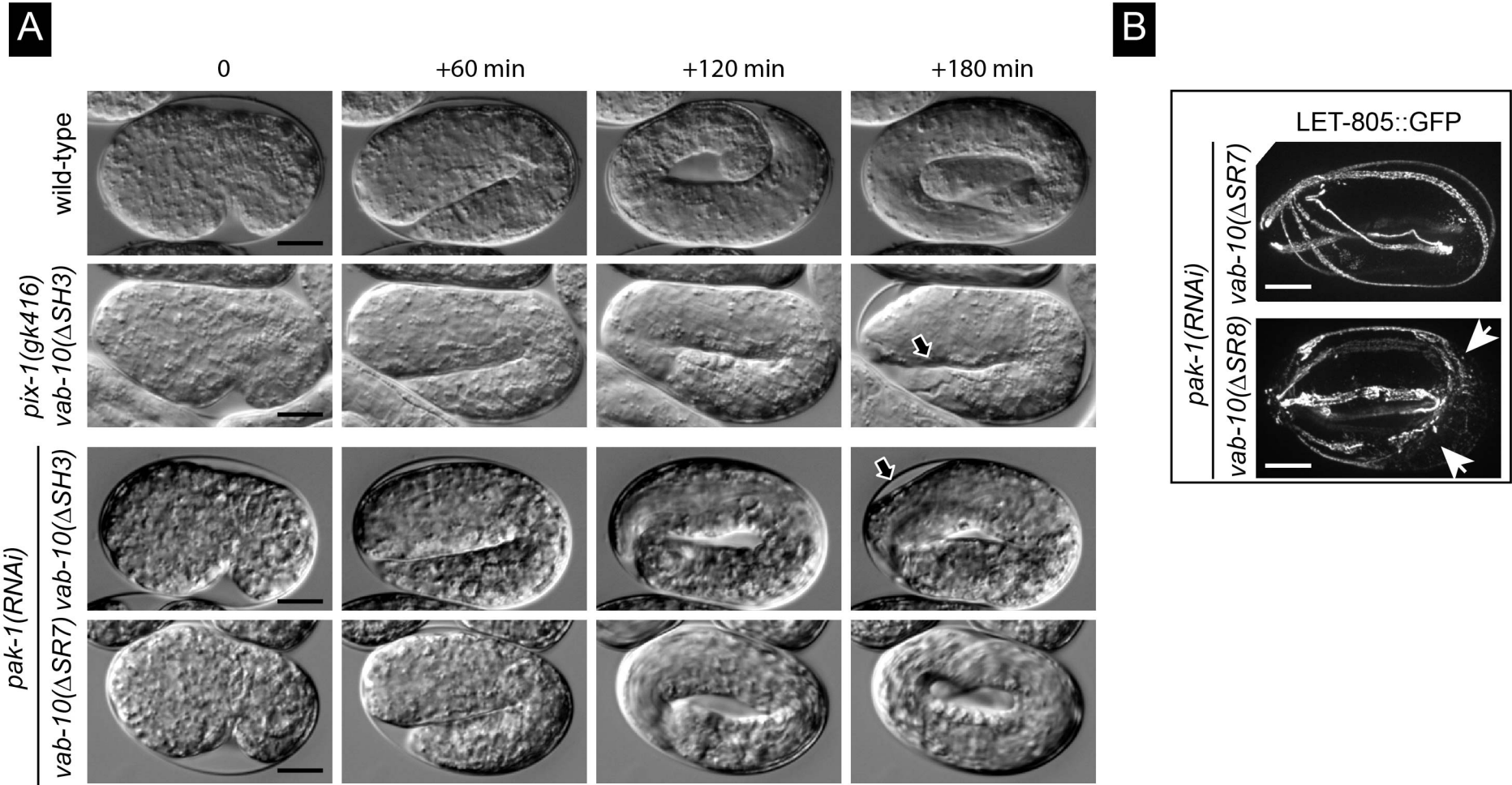
A
0
+60 min
+120 min
+180 min
wild-type
pix-1(gk416)
vab-10(ΔSH3)
pak-1(RNAi)
vab-10(ΔSH3)
vab-10(ΔSR7)
B
LET-805::GFP
pak-1(RNAi)
vab-10(ΔSR7)
vab-10(ΔSR8)

Figure S2

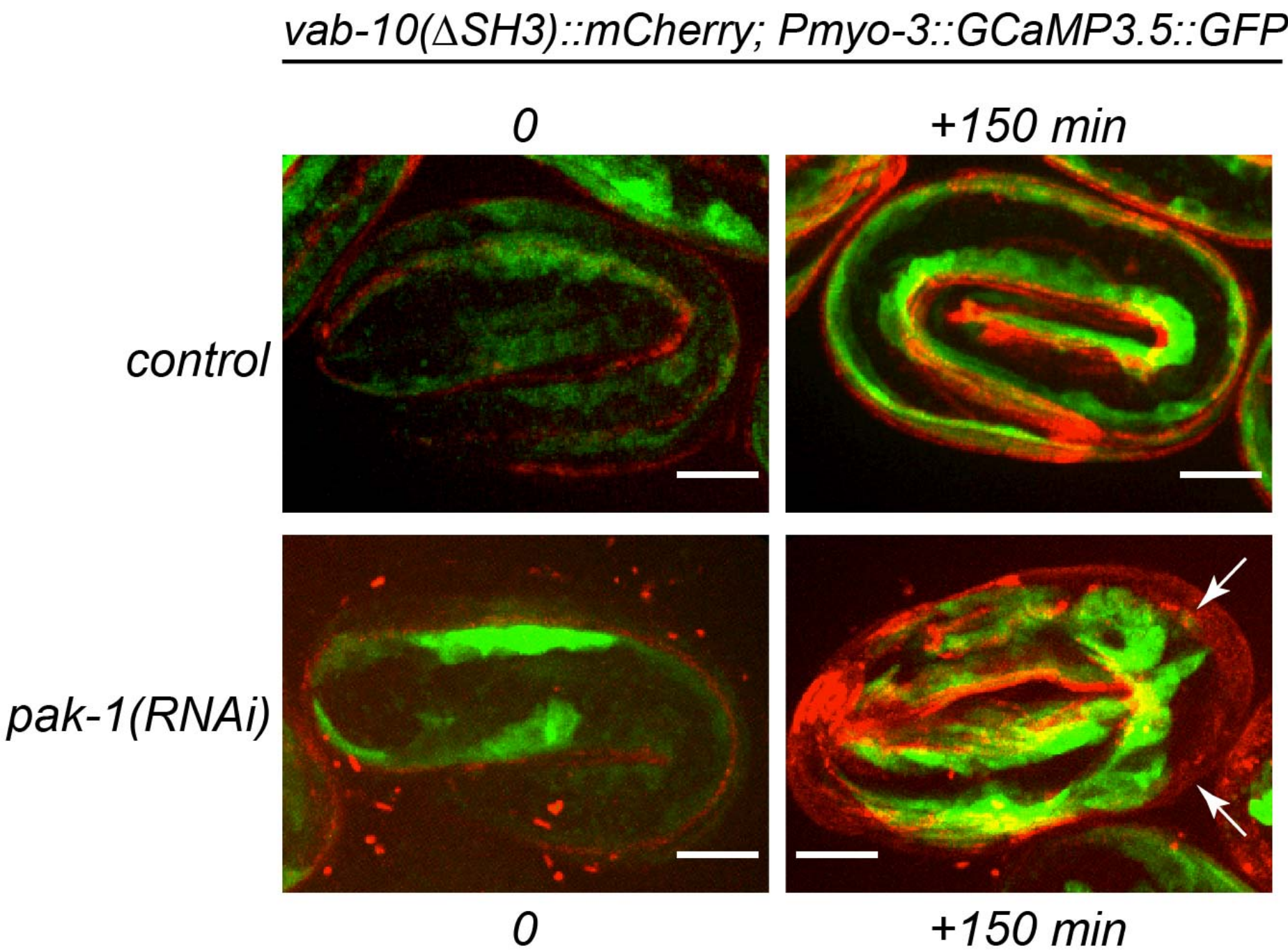
vab-10(ΔSH3)::mCherry; Pmyo-3::GCaMP3.5::GFP
0
+150 min
control
pak-1(RNAi)
0
+150 min

Figure S3

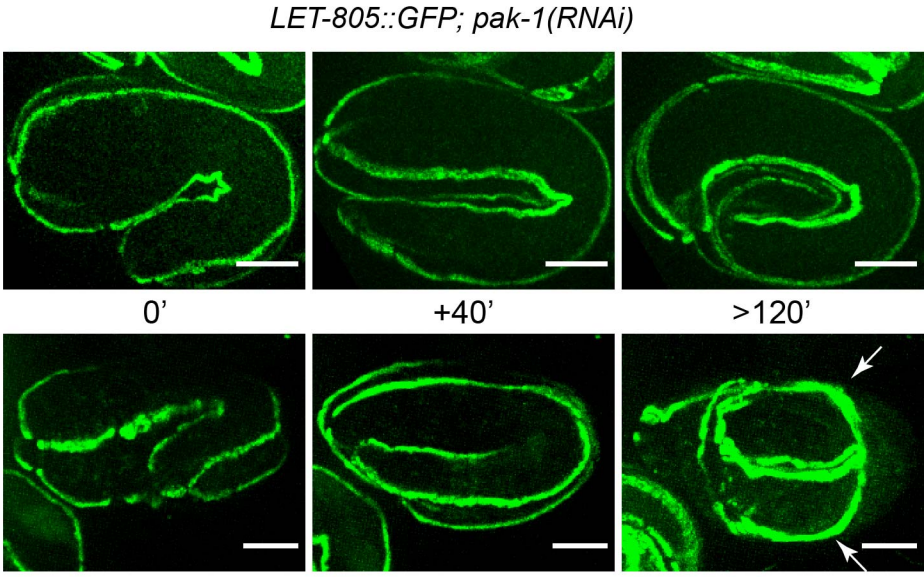

Figure S4

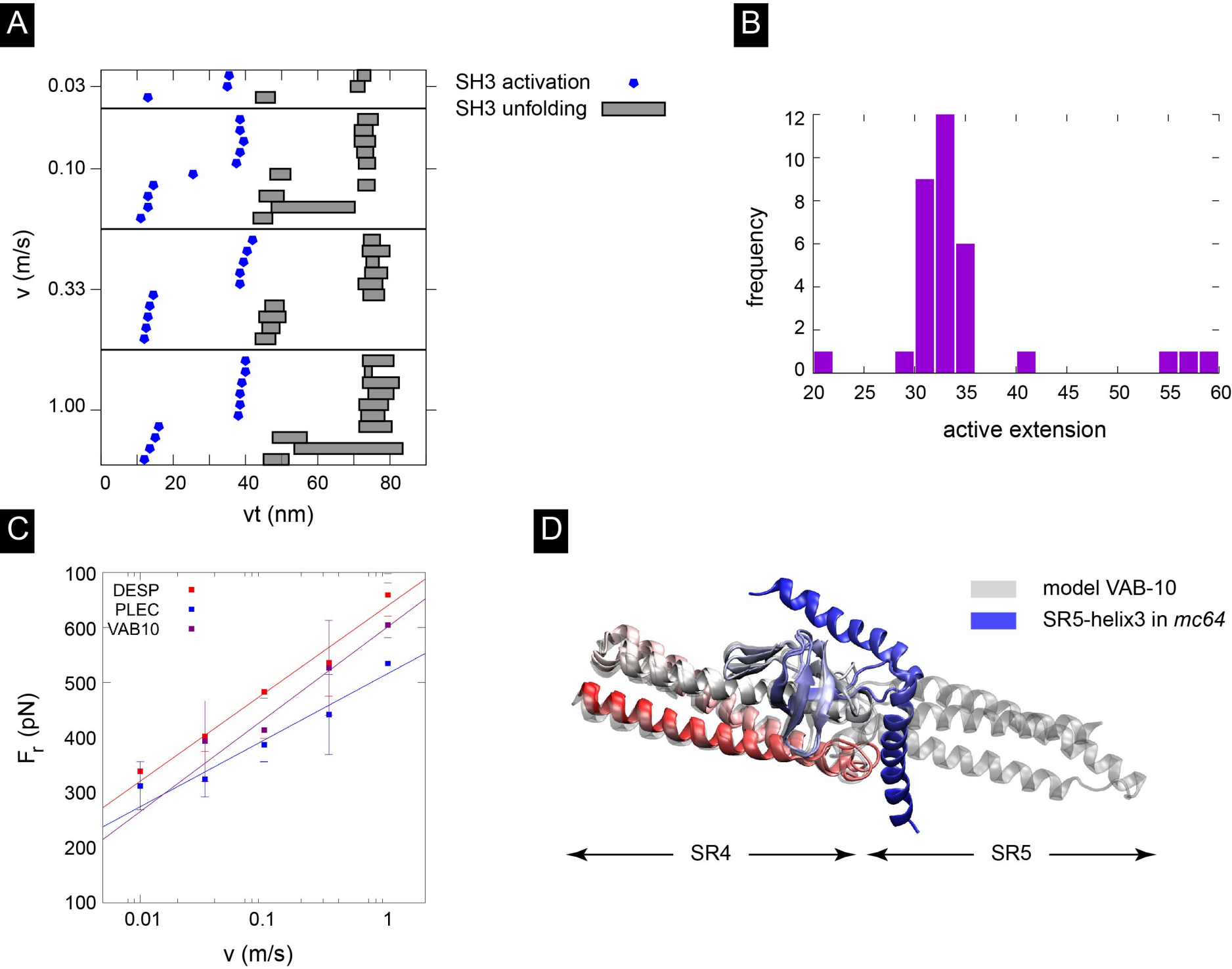
A
SH3 activation
SH3 unfolding
v (m/s)
0.03
0.10
0.33
1.00
0
20
40
60
80
vt (nm)
B
frequency
active extension
0
2
4
6
8
10
12
20
25
30
35
40
45
50
55
60
C
DESP
PLEC
VAB10
F_r (pN)
100
200
300
400
500
600
100
0.01
0.1
1
v (m/s)
D
model VAB-10
SR5-helix3 in *mc64*
SR4
SR5

Table 1

A genotype*, #	Viable	Emb let	BMD
wild-type	98.7%	1.3%	0.0%
vab-10A::mCherry=vab-10(mc100)	98.3%	1.7%	0.0%
vab-10[SH3(ΔS866)]=vab-10(mc55)	98.6%	1.4%	0.0%
vab-10[SH3(ΔPSVV_865-868)]=vab-10(mc56)	96.3%	2.2%	1.5%
vab-10(ΔSH3)=vab-10(mc62)	91.1%	8.4%	0.5%
vab-10[SH3(W852L)]=vab-10(mc70)	99.5%	0.5%	0.0%
vab-10[SH3(W852R)]=vab-10(mc79)	99.4%	0.6%	0.0%
vab-10[SR4(C729A)]=vab-10(mc80)	98.0%	2.0%	0.0%
vab-10[SH3(C826A)]=vab-10(mc81)	98.7%	1.3%	0.0%
vab-10A(ΔSH3)::mCherry=vab-10(mc109)	92.4%	6.8%	0.8%
vab-10(ΔSR5h1-h2)=vab-10(mc64)	0.0%	100%	0.0%
vab-10(ΔSR7)=vab-10(mc97)	96.8%	3.2%	0.0%
vab-10(ΔSR8)=vab-10(mc98)	95.9%	3.7%	0.4%

B	wild-type			*vab-10(e698)*			*vab-10(ΔSH3)*		
genotype*, #	Viable	Emb let	BMD	Viable	Emb let	BMD	Viable	Emb let	BMD
pak-1(RNAi)	99.1%	0.6%	0.3%	98.5%	1.5%	0.0%	0.9%	99.1%	0.0%
pak-1(ok448)	98.4	1.2%	0.4%	-	-	-	0.0%	100%	0.0%
pak-1(tm403)	96.4%	3.6%	0.0%	-	-	-	35.6%	43.4%	21.0%
git-1(tm1962)	98.1%	1.9%	0.0%	-	-	-	2.0%	98.0%	0.0%
crt-1(RNAi)	99.0%	1.0%	0.0%	52.4%	46.9%	0.7%	57.0%	11.0%	32.0%
mec-8(RNAi)	97.4%	2.6%	0.0%	62.2%	34.7%	3.1%	55.3%	39.3%	5.4%

C	*vab-10[SH3(W852L)]*			*vab-10[SH3(W852R)]*			*vab-10[SR4(C729A)]*			*vab-10(ΔSR7)*			*vab-10(ΔSR8)*		
genotype*, #	Viable	Emb let	BMD	Viable	Emb let	BMD	Viable	Emb let	BMD	Viable	Emb let	BMD	Viable	Emb let	BMD
pak-1(RNAi)	-	-	-	-	-	-	-	-	-	95.4%	4.6%	0.0%	10.8%	50.5%	39.1%
pak-1(ok448)	99.8%	0.2%	0.0%	99.8%	0.2%	0.0%	99.8%	0.2%	0.0%	67.0%	5.9%	27.1%	0.0%	100%	0.0%
pak-1(tm403)	99.5%	0.3%	0.2%	99.7%	0.3%	0.0%	-	-	-	-	-	-	-	-	-

Foonotes

* Viability judged 24 hours after egg-laying; Emb let, embryonic lethality; BMD, important body morphology defects

Sample size was above 700 except for *crt-1* and *mec-8* (part B) for which it was between 150 and 200

Table S1

Strain Name	Genotype	Method
N2	*Wild-type*	CGC
ML1949	*vab-10(ju281)/hT2 [bli-4(e937) let-?(q782) qIs48]I*	Genetic cross
ML2353	*vab-10(mc55[SH3(ΔS866)]I*	CRISPR/Cas9
ML2354	*vab-10(mc56[SH3(ΔPSVV_865-868)]I*	CRISPR/Cas9
ML2397	*vab-10(mc62[ΔSH3_820-873]I*	CRISPR/Cas9
ML2470	*vab-10(mc64[ΔSR5h1-h2_741-819])/hT2 [bli-4(e937) let-?(q782) qIs48]I*	CRISPR/Cas9
ML2485	*vab-10(mc70[SH3(W852L)]I*	CRISPR/Cas9
ML2501	*let-805(mc73[let-805::gfp])III*	CRISPR/Cas9
ML2527	*vab-10(mc79[SH3(W852R)]I*	CRISPR/Cas9
ML2528	*vab-10(mc80[SR4(C729A)]I*	CRISPR/Cas9
ML2529	*vab-10(mc81[SH3(C826A)]I*	CRISPR/Cas9
ML2537	*vab-10(mc44)/hT2 [bli-4(e937) let-?(q782) qIs48]I*	Genetic cross
ML2538	*vab-10(h1356)/hT2 [bli-4(e937) let-?(q782) qIs48]I*	Genetic cross
ML2550	*git-1(mc86[git-1::histag::2xpreCissionCleavageSite::gfp])X*	*Vuong-Brender et al 2017*
ML2563	*vab-10(mc62[ΔSH3_820-873]I; git-1(mc86[git-1::histag::2xpreCissionCleavageSite::gfp])X*	Genetic cross
ML2567	*vab-10(mc80[SR4(C729A)]I; pak-1(ok448)X*	Genetic cross
ML2583	*vab-10(mc79[SH3(W852R)]I; pak-1(tm403)X*	Genetic cross
ML2584	*vab-10(mc70[SH3(W852L)]I; pak-1(tm403)X*	Genetic cross
ML2587	*vab-10(mc62[ΔSH3_820-873]I; let-805(mc73[let-805::gfp])III*	Genetic cross
ML2588	*vab-10(mc70[SH3(W852L)]I; pak-1(ok448)X*	Genetic cross
ML2589	*vab-10(mc79[SH3(W852R)]I; pak-1(ok448)X*	Genetic cross
ML2596	*vab-10(mc62[ΔSH3_820-873]I; git-1(tm1962)X*	Genetic cross
ML2599	*vab-10(mc97[ΔSR7_987-1086]I*	CRISPR/Cas9
ML2600	*vab-10(mc100[vab-10A::mCherry + LoxP]I*	CRISPR/Cas9
ML2601	*vab-10(mc98[ΔSR8_1109-1211]I*	CRISPR/Cas9
ML2634	*pix-1(mc107[pix-1::VC_155-238])X*	CRISPR/Cas9
ML2639	*vab-10(mc97[ΔSR7_987-1086]I; let-805(mc73[let-805::gfp])III*	Genetic cross
ML2640	*vab-10(mc98[ΔSR8_1109-1211]I; let-805(mc73[let-805::gfp])III*	Genetic cross
ML2641	*vab-10(mc100[vab-10A::mCherry + LoxP]I; let-805(mc73[let-805::gfp])III*	Genetic cross
ML2645	*vab-10(mc100[vab-10A::mCherry + LoxP]I; git-1(mc86[git-1::histag::2xpreCissionCleavageSite::gfp])X*	Genetic cross
ML2666	*vab-10(mc109[vab-10A(ΔSH3_820-873)::mCherry + LoxP]I*	CRISPR/Cas9
ML2671	*vab-10(mc64[ΔSR5h1-h2_741-819])/hT2 [bli-4(e937) let-?(q782) qIs48]I; let-805(mc73[let-805::gfp])III*	Genetic cross
ML2672	*vab-10(mc64[ΔSR5h1-h2_741-819])/hT2 [bli-4(e937) let-?(q782) qIs48]I; git-1(mc86[git-1::histag::2xpreCissionCleavageSite::gfp])X*	Genetic cross
ML2680	*vab-10(mc109[vab-10A(ΔSH3_820-873)::mCherry + LoxP]I; let-805(mc73[let-805::gfp])III*	Genetic cross
ML2682	*vab-10(mc109[vab-10A(ΔSH3_820-873)::mCherry + LoxP]I; goeIs3 [myo-3p::SL1::GCamP3.35::SL2::unc54 3'UTR + unc-119(+)]*	Genetic cross
ML2728	*git-1(mc110[git-1::VN_1-173])X*	CRISPR/Cas9
ML2735	*git-1(mc110[git-1::VN_1-173]), pix-1(mc107[pix-1::VC_155-238])X*	Genetic cross
ML2760	*vab-10(mc114[vab-10A::VC_155-238])I*	CRISPR/Cas9
ML2761	*vab-10(mc114[vab-10A::VC_155-238])I; git-1(mc110[git-1::VN_1-173])X*	Genetic cross
ML2764	*vab-10(mc109[vab-10A(ΔSH3_820-873)::mCherry + LoxP]I; mup-4(mc121[mup-4::gfp + LoxP)]III*	Genetic cross
ML2799	*vab-10(mc123[vab-10B::gfp + LoxP]I*	CRISPR/Cas9
ML2800	*vab-10(mc124[vab-10B((ΔSH3_820-873)_gfp]I*	CRISPR/Cas9

Table S2

Gene (allele)	**SG sequence (5'-3') without PAM**
vab-10(mc62)	GCGGTAACCTTGATCGGATG(1st site) GTGAGACGAGCATCAGTCGG (2nd site)
vab-10(mc64)	GTCGGAAGCCTCCTCCATAA (1st site) GTGCAAGCATCTCACCACTC(2nd site)
vab-10(mc55 & 56)	GAGGGACAAGTCCCATCAG
vab-10(mc70 & 79)	GGACGATTCGTGACATCTC
vab-10(mc80)	GCGTTAAGCAAGTGCCTTG
vab-10(mc81)	TCGGAATAGTCACAGAGTG
git-1(mc86) - GFP knockin	AAACTTCGCCTGATTATCA
git-1(mc110) – Venus 1st half knockin	AAACTTCGCCTGATTATCA
vab-10(mc97)	GAGTTGCTGAAGAAGTTGG
vab-10(mc98)	CTCAAGGTGAGCAAGTTGG
pix-1(mc107) - Venus 2nd half knockin	AGTTCCAGTACTCCAAGAA
vab-10A(mc100 & mc109) - mCherry knockin	GCGTGGGCACGTAAGCAAT
vab-10A(mc114) - Venus 2nd half knockin	GCGTGGGCACGTAAGCAAT
vab-10B(mc123) - GFP knockin	ACTTTGAAGACGATGATGA
vab-10B(mc124) - GFP knockin	CGGCTGCAGATTTGGCACAG
let-805(mc73) - GFP knockin	GAAAATTTCCAGAGATTAA
mup-4(mc121) - GFP knockin	ATAGTTGACTTCTTCTGCTT